Large-Aspect-Ratio Structures in Simulated Ocean Surface Boundary Layer Turbulence under a Hurricane

CLIFFORD WATKINS[a] AND DANIEL B. WHITT[b]

[a] *Department of Marine and Coastal Sciences, Rutgers, The State University of New Jersey, New Brunswick, New Jersey*
[b] *Climate and Global Dynamics Laboratory, National Center for Atmospheric Research, Boulder, Colorado*

(Manuscript received 18 June 2020, in final form 29 September 2020)

ABSTRACT: A large-eddy simulation (LES) initialized and forced using observations is used to conduct a process study of ocean surface boundary layer (OSBL) turbulence in a 2-km box of ocean nominally under Hurricane Irene (2011) in 35 m of water on the New Jersey shelf. The LES captures the observed deepening, cooling, and persistent stratification of the OSBL as the storm approaches and passes. As the storm approaches, surface-intensified Ekman-layer rolls, with horizontal wavelengths of about 200 m and horizontal-to-vertical aspect and velocity magnitude ratios of about 20, dominate the kinetic energy and increase the turbulent Prandtl number from about 1 to 1.5 due partially to their restratifying vertical buoyancy flux. However, as the storm passes, these rolls are washed away in a few hours due to the rapid rotation of the wind. In the bulk OSBL, the gradient Richardson number of the mean profiles remains just above (just below) 1/4 as the storm approaches (passes). At the base of the OSBL, large-aspect-ratio Kelvin–Helmholtz billows, with Prandtl number below 1, intermittently dominate the kinetic energy. Overall, large-aspect-ratio covariance modifies the net vertical fluxes of buoyancy and momentum by about 10%, but these fluxes and the analogous diffusivity and viscosity still approximately collapse to time-independent dimensionless profiles, despite rapid changes in the forcing and the large structures. That is, the evolutions of the mean temperature and momentum profiles, which are driven by the net vertical flux convergences, mainly reflect the evolution of the wind and the initial ocean temperature profile.

KEYWORDS: Coastal flows; Turbulence; Boundary layer; Oceanic mixed layer; Large eddy simulations

1. Introduction

Observations (e.g., Savelyev et al. 2018b) and simulations (e.g., Hamlington et al. 2014) show that ocean surface boundary layer (OSBL) turbulence sometimes includes a continuum of horizontal length scales characterized by a negative power spectral slope without a peak in variance near the length scale of the OSBL depth. In particular, prominent large-aspect-ratio[1] structures with horizontal scales larger than the OSBL depth coexist with more isotropic structures with scales similar to and smaller than the OSBL depth. Generically, these large-aspect-ratio structures can be generated in the OSBL by extracting energy from the mean profile (e.g., via an instability) and via nonlinear transfers of variance from other scales of variability, or they can propagate into the OSBL from below. Prior work has loosely classified observed large-aspect-ratio structures into a few categories: 1) wind/wave/buoyancy-driven Langmuir circulations that are characterized by horizontally anisotropic rolls and streaks approximately aligned with the wind vector and perpendicular to surface wave crests (Langmuir 1938; Leibovich 1983; Smith 1992; Thorpe 2004; Kukulka et al. 2009), mostly with cross-roll length scales less than 4 times the OSBL depth but with some notable larger exceptions (Marmorino et al. 2005; Gargett et al. 2004; Sundermeyer et al. 2014; Gargett and Savidge 2020); 2) internal waves (Elachi and Apel 1976; Wijesekera and Dillon 1991; Shaun-Johnston and Rudnick 2009); 3) stratified shear instabilities such as the Kelvin–Helmholtz (KH) mode (Seim and Gregg 1994; Chang et al. 2016); and 4) submesoscale vortex and frontal dynamics (Munk et al. 2000; Savelyev et al. 2018a; D'Asaro et al. 2018; Marmorino and Chen 2019).

Other boundary layers also contain prominent large-aspect-ratio structures, which exhibit some similarities to their OSBL cousins. For example, numerous observations reveal roll vortices and associated streaks characteristic of shear instabilities in the atmospheric boundary layer (ABL) (Lemone 1973, 1976; Etling and Brown 1993; Young et al. 2002). In addition, laboratory measurements and direct numerical simulations reveal long streaks extending up to 10 times the BL height approximately aligned with the shear in high-Reynolds number wall-bounded flows with and without rotation and/or stratification (Tatro and Mollo-Christensen 1967; Marusic et al. 2010; Smits et al. 2011; Hutchins et al. 2012; Sous et al. 2013; Deusebio et al. 2014).

However, the role of large-aspect-ratio structures in OSBL turbulence and their implications for larger-scale ocean dynamics remains to be fully understood. Here, we build understanding

[1] Unless otherwise specified, we define large-aspect ratio to mean that the characteristic horizontal length scale is larger than the characteristic vertical length scale (no specific physical process is implied). Confusingly, many features of interest are also elongated and anisotropic in the horizontal plane. Hence, unless otherwise specified, the characteristic horizontal length scale of a structure refers to the shortest possible characteristic horizontal scale that can be derived.

Supplemental information related to this paper is available at the Journals Online website: https://doi.org/10.1175/JPO-D-20-0134.s1.

Corresponding author: Daniel B. Whitt, dwhitt@ucar.edu

DOI: 10.1175/JPO-D-20-0134.1

by reporting on a large-eddy simulation (LES) that models the rapid turbulent entrainment and sea surface temperature (SST) cooling observed on the New Jersey shelf during the passage of Hurricane Irene in 2011 (Glenn et al. 2016; Seroka et al. 2016) and contains vigorous large-aspect-ratio structures, which participate with smaller-scale turbulence in driving the entrainment and surface cooling.

Many previous studies have used LES to investigate transient and unsteady OSBL dynamics. LES provides a local perspective on OSBL turbulence that is generated by the surface forcing, dynamical instabilities and nonlinear transfers across the resolved scales, without the convoluting effects of lateral advection or propagation from remote locations or local transfers of energy from scales that are unresolved on the grid. However, only a few studies have used LES to study OSBL turbulence including horizontal wavelengths greater than 10 times the OSBL depth. Most of these studies have used large-aspect-ratio domains to study the interactions between submesoscale vortex and frontal dynamics and smaller-scale turbulence (e.g., Skyllingstad and Samelson 2012; Hamlington et al. 2014; Sundermeyer et al. 2014; Taylor 2016; Smith et al. 2016; Whitt and Taylor 2017; Skyllingstad et al. 2017; Callies and Ferrari 2018; Sullivan and McWilliams 2018, 2019). Comparatively little work has been devoted to investigating the role of such large-aspect-ratio structures in OSBLs forced simply by wind, before considering buoyancy and/or surface gravity wave effects. However, previous LES studies have noted interactions between surface boundary layer turbulence and short internal waves (Polton et al. 2008; Czeschel and Eden 2019). Sullivan et al. (2012) noted that it was necessary to use a 1500-m-wide domain (12.5 times the maximum OSBL depth) in order to resolve some spontaneously generated internal waves under hurricane forcing. Others (Sundermeyer et al. 2014; Skyllingstad et al. 2017) found large-aspect-ratio Ekman-layer rolls with horizontal scales 5–10 times the OSBL depth in both observations and LES, regardless of whether surface wave effects were included in the LES. Although ABL LES is limited by the similar computational challenges, previous studies have repeatedly simulated large structures approximately aligned with the geostrophic flow in the Ekman ABL (e.g., Moeng and Sullivan 1994; Khanna and Brasseur 1998; Fang and Porté-Agel 2015). However, it is still not well known how large-aspect-ratio structures contribute to the net fluxes and mean evolution of the OSBL under time-variable wind. But, it seems likely that large structures are important in some circumstances.

The purpose of this paper is to describe the simulated large-aspect-ratio structures and their role in OSBL turbulence under a hurricane in a large-aspect-ratio oceanic domain in which the OSBL depth ranges from 1/200 to 1/55 the horizontal domain length. The simulation is realistic in that it is initialized with observed temperature and salinity vertical profiles just before the storm and forced by a time-dependent 3-hourly surface wind stress, heat flux, and penetrative radiative heating derived from atmospheric reanalysis. On the other hand, the simulation is idealized in that all other processes are omitted, including the effects of ocean surface gravity waves and the larger-scale ocean circulation. The expectation is not that these other processes or their interactions with wind- and buoyancy-forced OSBL turbulence are not important. Rather, the expectation is that it is necessary to study these different processes both in isolation and in combination to obtain a full understanding of OSBL dynamics. This paper is a step toward that broader goal. After a description of the model, the results include two parts: the first is a descriptive analysis of the life cycle and characteristics of the simulated large-aspect-ratio structures. The second demonstrates how the evolution of the large-scale structures relates to and impacts the evolution of the mean profiles of momentum and buoyancy via the turbulent vertical fluxes that drive the evolution of the mean profiles.

2. Model configuration

a. Model description and initial conditions

The numerical model is similar to that used in Whitt and Taylor (2017) [and described in more detail by Taylor (2008)]. Briefly, the evolution of the resolved flow is obtained by time-stepping the rotating Boussinesq equations on a traditional f plane with Coriolis frequency $f = 9.3 \times 10^{-5}\,\mathrm{s}^{-1}$ using a mixed method, in which the Crank–Nicholson scheme advances the vertical viscous/diffusive terms, a third-order Runge–Kutta scheme advances all other terms, and the projection method is used to enforce incompressibility and update the pressure. Spatial derivatives are discretized using a pseudospectral approach in the horizontal and second-order central differences in the vertical. The fluid density ρ and buoyancy $b = -g\rho/\rho_0$ depend on both temperature and salinity via a linear equation of state $\rho = \rho_0[1 + \alpha(T - T_0) + \beta(S - S_0)]$, where $\rho_0 = 1022.8\,\mathrm{kg\,m}^{-3}$, $T_0 = 17.0°\mathrm{C}$, $S_0 = 31.5$ psu, $\alpha = -0.000\,281\,°\mathrm{C}^{-1}$, and $\beta = 0.000\,766\,\mathrm{psu}^{-1}$, and $g = 9.81\,\mathrm{m\,s}^{-2}$. Subgrid-scale (SGS) momentum fluxes are obtained using a modified Smagorinsky approach (Kaltenbach et al. 1994). The subgrid-scale fluxes of salt and temperature are represented by a down-gradient diffusion, where the diffusivities of heat and salt are equal but vary spatially and temporally with the subgrid-scale viscosity and Prandtl number, that is $\kappa_{\mathrm{SGS}} = \nu_{\mathrm{SGS}}\mathrm{Pr}_{\mathrm{SGS}}^{-1}$. As in Whitt and Taylor (2017), $\mathrm{Pr}_{\mathrm{SGS}}^{-1} = 1/(1 + \mathrm{Ri}_{\mathrm{GS}}/0.94)^{1.5}$ (Anderson 2009) and the gridscale gradient Richardson number $\mathrm{Ri}_{\mathrm{GS}} = \delta z \delta b/(\delta u^2 + \delta v^2)$, where δ denotes the difference between two vertically adjacent grid cells and u and v denote the horizontal components of the velocity vector.

The numerical solution is obtained in a horizontally periodic domain that is 1958 m × 1958 m × 35 m and spanned by a mesh with 2304 × 2304 × 85 grid points that are evenly spaced 0.85 m × 0.85 m × 0.42 m apart. A study of the sensitivity of the LES solutions to the domain size is not pursued here. However, we note that horizontal domains of 245, 122, and 41 m with the same horizontal and vertical grid spacings were also attempted. In the larger two of three domains, the simulations revealed dominant domain-scale structures and intermittency in the statistics, both of which were deemed undesirable. These issues were somewhat mitigated in the smallest domain, but the statistics in that case are not very robust with so few points.

The time step is varied dynamically so that the Courant number remains sufficiently small and the time stepping

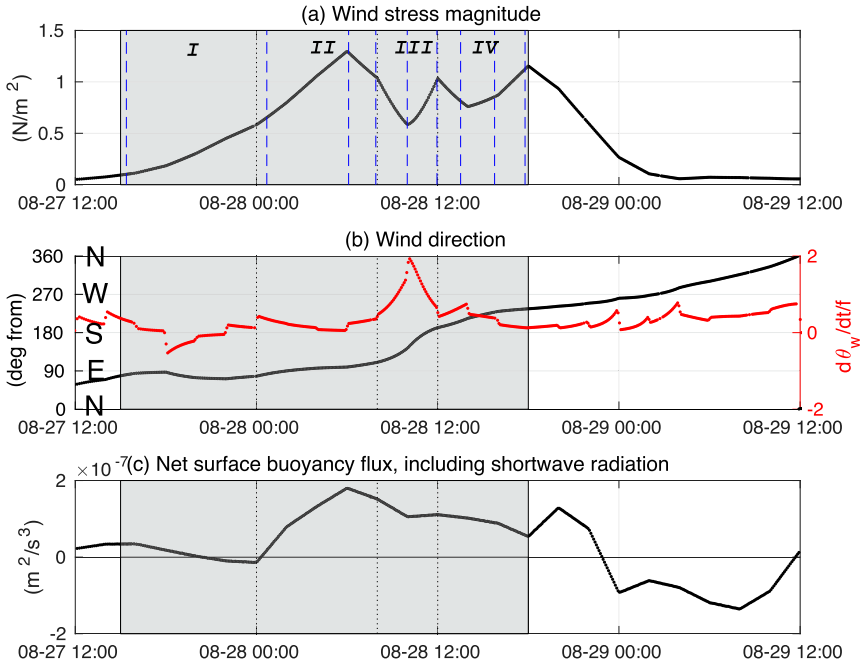

FIG. 1. Ocean surface fluxes during the storm. The surface stress has (a) magnitude $|\boldsymbol{\tau}|$ and (b) direction θ_w (left axis) and rate of rotation normalized by the Coriolis frequency $d\theta_w/dt/f$ (right axis). (c) The net surface buoyancy flux, which is (atypically) injecting buoyancy into the ocean during most of the storm, includes the penetrating shortwave, net longwave, latent, and sensible heat fluxes. Surface freshwater/salinity fluxes are set to zero for simplicity. This paper focuses on the gray-shaded time period and separates that period into four phases, as described in the text.

scheme remains stable. Due to the strong currents during the storm, the time step drops below 0.15 s late in the storm. Hence, the simulation requires about 370 000 time steps to reach the end of phase IV in Fig. 1a. The depth of the domain is chosen to be approximately the same as the ocean bottom depth roughly 100 km east of Cape May, New Jersey (about half way from the coast to the shelf break), where glider observations of temperature and salinity profiles were available before and during the storm; the glider maintained station-keeping operations near the 40-m isobath as shown in Fig. 2 with surfacing for upload of data every 3 h (Glenn et al. 2016).

The velocity field is initialized with a small-amplitude random kick in each grid cell with root-mean-square of order $10^{-4}\,\mathrm{m\,s^{-1}}$, and the temperature and salinity are initialized with horizontally uniform profiles that are defined by analytic functions designed to approximately match observed temperature and salinity profiles obtained by a glider on the New Jersey shelf just before the storm (Fig. 3) [for details about the observations, see Glenn et al. (2016)]. The simulation begins at 0000 UTC 27 August 2011 and runs through 1800 UTC 29 August, but the atmospheric forcing is modest until 1500 UTC 27 August, when our analysis begins (Fig. 1).

b. *Atmospheric forcing and boundary conditions*

The surface and bottom boundary conditions for vertical velocity are $w = 0$; temperature, salinity, and horizontal velocity are horizontally uniform but time-dependent vertical gradients. At the top, the vertical gradients of horizontal velocity, e.g., $\nu_{\mathrm{SGS}}\partial\mathbf{u}/\partial z = \boldsymbol{\tau}/\rho_0$ where $\nu_{\mathrm{SGS}} = 10^{-6}\,\mathrm{m^2\,s^{-1}}$, and temperature are defined by 3-hourly surface wind stress and heat fluxes (excluding penetrating shortwave) derived from a regional ocean model published by Glenn et al. (2016) (Fig. 1). That regional ocean model in Glenn et al. (2016) is initialized from a state obtained via data assimilation and forced by the 3-hourly/12-km resolution reanalysis from the North American Mesoscale forecast model, and the surface fluxes are calculated using the COARE algorithm (Fairall et al. 2003). As in the regional ocean model of Glenn et al. (2016), shortwave radiation penetrates and acts as an interior heat source in the LES that follows a modified Jerlov type II two-component exponential profile (Paulson and Simpson 1977) with the first e-folding depth scale $\zeta_1 = 5$ m instead of 1.5 m to avoid a collapse of turbulence near the surface under stabilizing buoyancy forcing and weak wind before the storm. This approach is ad hoc and may need to be reconsidered in future work, but it is plausibly justified based on observations that the top few meters are sometimes more turbulent than expected from the wind stress and buoyancy flux alone due to surface wave effects (e.g., Anis and Moum 1995).

To aid in the latter description, we separate the forcing into four phases of interest as shown in Fig. 1a. In phase I, there is a period of rising but modest ($|\boldsymbol{\tau}| < 0.5\,\mathrm{N\,m^{-2}}$) and consistently easterly wind as the storm approaches from the south along the U.S. east coast. Then, in phase II there is a period of stronger

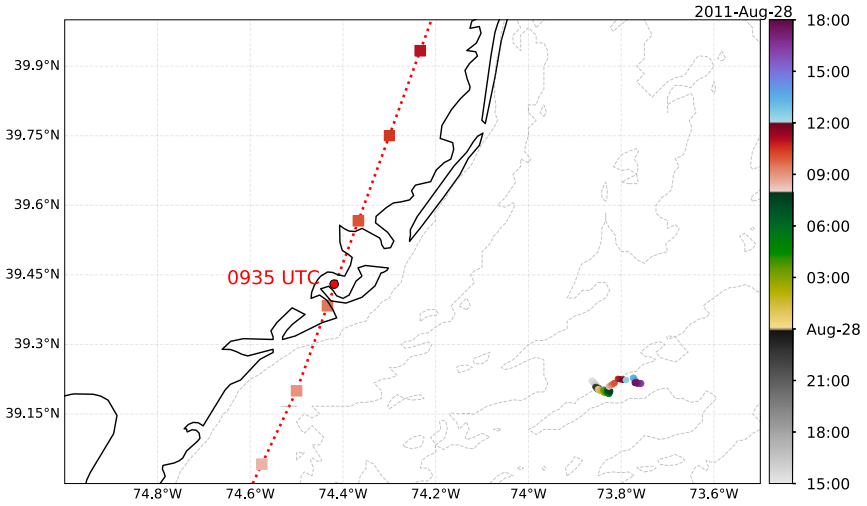

FIG. 2. The track of a profiling buoyancy glider (small dots) and bathymetry contours (dotted lines every 10 m). Color indicates the time (UTC), which is separated into four phases: I (black), II (green), III (red), and IV (blue) (see Fig. 1). The approximate location of the hurricane's eye is indicated by squares, which are spaced every 30 min and are colored to indicate the time, similar to the glider track. The red dot on the hurricane track indicates the time and location of landfall (Glenn et al. 2016).

winds from the east ($|\boldsymbol{\tau}| > 0.5\,\mathrm{N\,m^{-2}}$), which is punctuated by the maximum wind stress ($1.2\,\mathrm{N\,m^{-2}}$) at 0600 UTC 28 August. Phase III includes the eye passage, when winds are strong but weaker than the maximum ($1 > |\boldsymbol{\tau}| > 0.5\,\mathrm{N\,m^{-2}}$) and the stress vector rotates rapidly. Since the LES domain is situated to the right of the eye track, the wind stress vector rotates clockwise from a westward stress (easterly winds) to a northeastward stress (southwesterly winds) as the eye passes (Fig. 1b). Finally, phase IV represents the period of strong and persistently southwesterly wind after the eye passes. The subsequent periods of decaying winds and low poststorm winds are not considered in this paper.

Atypically, the net heat flux is into the ocean during most of the storm and during almost all of 28 August (Fig. 1c). During phases II and III, as the wind ramps up and eventually the eye passes at about 0900 UTC 28 August, the turbulent heat and buoyancy fluxes and the corresponding vertical temperature gradient at the surface boundary of the LES are positive (injecting heat into the ocean) during nighttime (Figs. 1b,c). During phase IV and the remainder of 28 August after the eye passage, there are weak turbulent heat losses from the ocean and a negative surface temperature gradient at the top boundary of the LES, but solar radiation makes the net heat flux positive until nearly nightfall at roughly 0000 UTC 29 August. This unusual situation, in which the turbulent surface latent and sensible heat fluxes are into the ocean, is thought to have been caused by the rapid entrainment-driven ahead-of-eye cooling of the SST, which contributed to the observed rapid decay of the hurricane during this period (Glenn et al. 2016; Seroka et al. 2016).

Before proceeding, consider the relative importance of the surface buoyancy flux $F_b(0)$ (Fig. 1c) and momentum flux $\mathbf{F}_m(0) = \boldsymbol{\tau}/\rho_0$ for the OSBL turbulence using Monin–Obukhov similarity theory (e.g., Monin and Obukhov 1954; Businger et al. 1971; Lombardo and Gregg 1989). First, the Monin–Obukhov length $L_{\mathrm{MO}} = |\mathbf{F}_m(0)|^{3/2}/[k|F_b(0)|] > 300\,\mathrm{m}$, where $k = 0.4$ is the von Kármán constant. And, the boundary layer is only 10–30 m deep. So, the conditions are generally near neutral, that is $|z/L_{\mathrm{MO}}| < 0.1$ and the wind-driven turbulence is expected to be only modestly impacted by the stable surface buoyancy flux at all depths and throughout the duration of the analysis (i.e., the shaded gray area in Fig. 1).

During the analysis period reported here (the gray shaded area in Fig. 1), the bottom layer remains nearly motionless and stratified on average, and the magnitude of the bottom stress never exceeds $10^{-4}\,\mathrm{N\,m^{-2}}$, so the details of the bottom gradient conditions and the associated wall model are thought to be unimportant and omitted for brevity although the bottom may still be significant, e.g., due to the trapping of internal wave energy that might otherwise radiate downward in the open ocean.

3. Visualization and description

We begin by reporting the results of flow visualizations and describe the dominant large turbulent structures in the OSBL, which we separate from more quiescent water below by the depth of maximum stratification $z = -D_{N^2}$, where the stratification is defined by $\langle N^2\rangle_{x,y} = \langle \partial b/\partial z\rangle_{x,y}$ (here, $\langle\rangle_{x,y}$ denotes an average over the horizontal dimensions x and y). This section is separated into two parts to facilitate a description of the two types of large structure that are, conveniently, dominant at two distinct depth levels: the first is a discussion of the near-surface layer, and the latter is focused on the base of the OSBL (i.e., just above D_{N^2}).

a. *Near surface*

Plan views of the simulated currents at 5-m depth early on 28 August (the beginning of phase II) reveal striking anisotropic

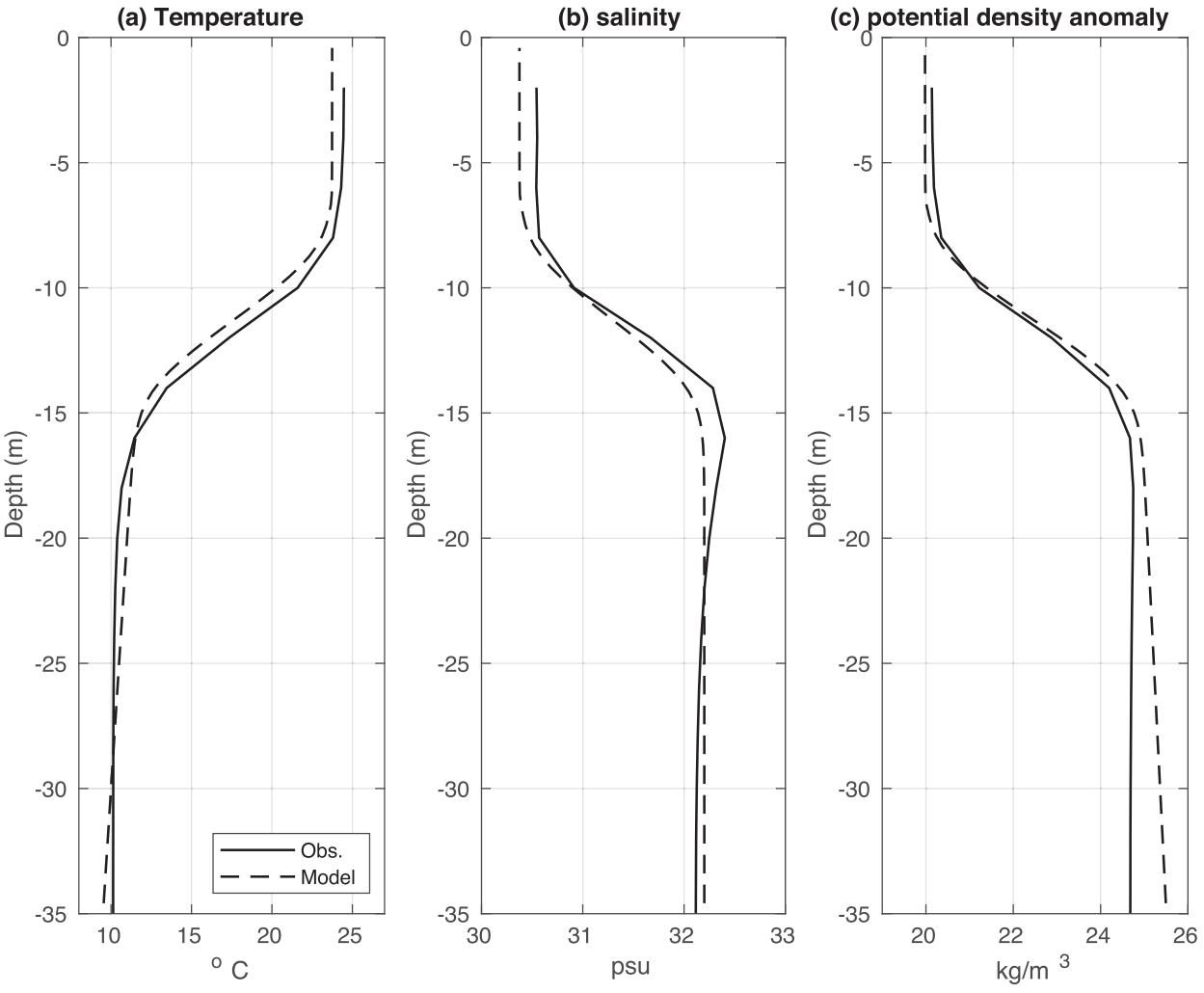

FIG. 3. A comparison between the modeled and observed (a) temperature, (b) salinity, and (c) potential density profiles just before the storm at 1200 UTC 27 Aug 2011, when the glider was at 39.24°N, 73.88°W.

streaks that are elongated in the wind direction (Fig. 4). We begin with a chronological description of the life cycle of these structures. Then we describe the spatial structure in more detail using vertical sections of several key variables in a streak–roll coordinate system.

It may be noted that the features are reminiscent of Ekman layer rolls [for stratified linear stability analysis, see Kaylor and Faller (1972), Brown (1972), and Asai and Nakasuji (1973); for atmospheric observations, see Lemone (1973, 1976); for recent oceanic perspective, see Sundermeyer et al. (2014), Duncombe (2017), and Skyllingstad et al. (2017)], but comparisons between the associated theory, prior observations, and the structures reported here are deferred to the discussion section.

1) CHRONOLOGY

To begin with, it is notable that it takes about 15–24 h for the streaks shown in Fig. 4 to first emerge as dominant features of the turbulence during phase I (which begins 15 h into the simulation at 1500 UTC 27 August), either because it takes this long for the wind to reach sufficient strength and/or because the motions take this long to achieve finite amplitude via another dynamic mechanism such as a linear instability. In particular, the power spectrum of kinetic energy as a function of time at 5-m depth and at large-scale wavelengths $\lambda > 3D_{N^2}$ exhibits approximately exponential growth in time $e^{t/\tau}$ with $\tau \sim 10^4$ s. At the same time, the wind stress magnitude and the associated magnitude of the mean wind-driven currents in the OSBL also increase approximately exponentially at about the same rate as the storm approaches. However, the largest of the large scales (~1 km) are energized somewhat more slowly than the smaller of the large scales (~0.1 km) (not shown; but the netCDF files with the spectra are published in Watkins and Whitt 2020). As a result, the fraction of the horizontal kinetic energy associated with wavelengths longer than 3 times $D_{N^2} \approx 10$ m is less than 25% of the total variance before 2000 UTC 27 August (Figs. 5a–c). In addition, the maxima in the radially integrated horizontal wavenumber spectra of both horizontal and vertical kinetic energy are both at about 0.1 cycles per meter

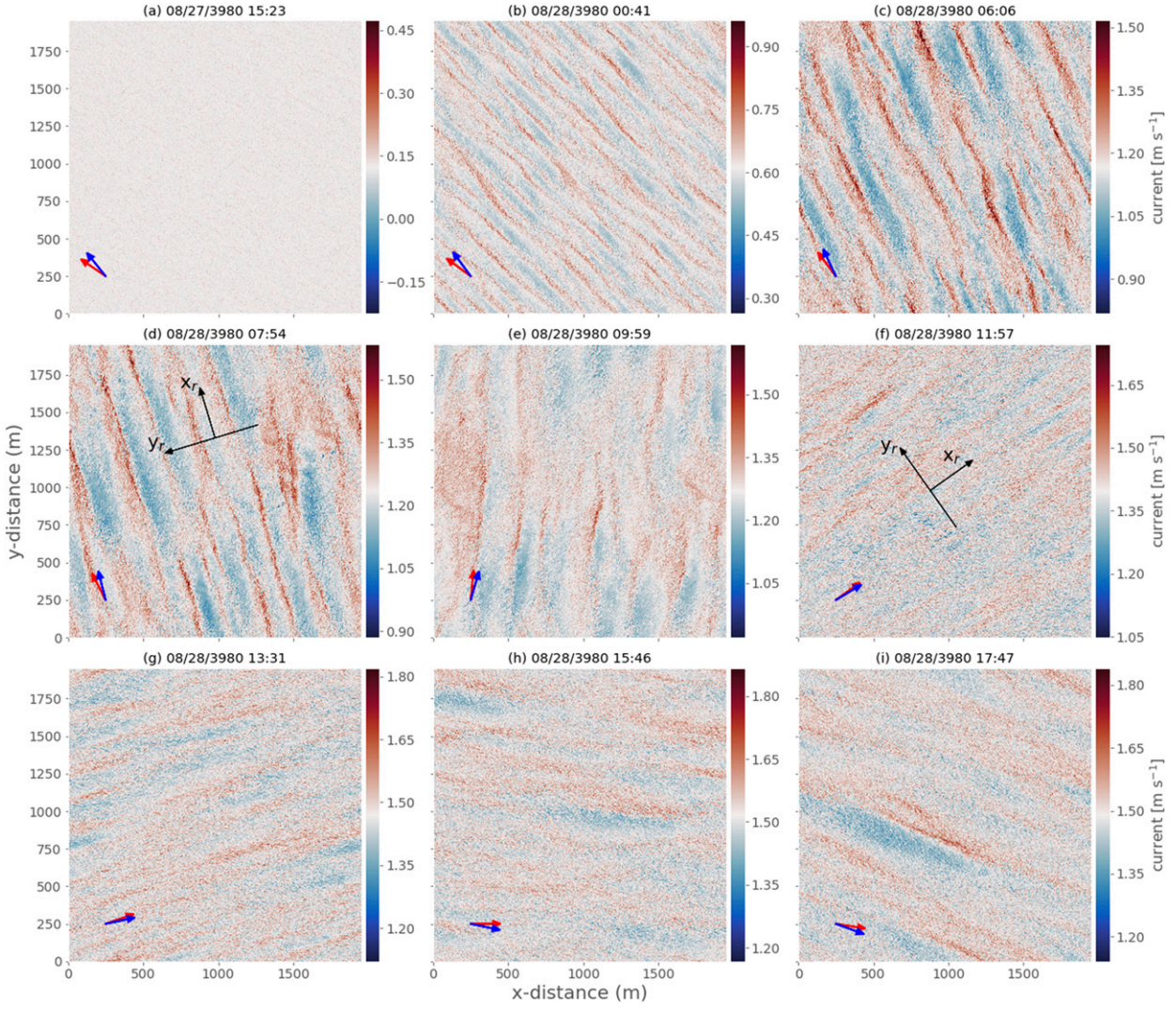

FIG. 4. Snapshots showing the speed of the horizontal current 5 m below the surface at nine times during phases (a) I, (b)–(d) II, (e),(f) III, and (g)–(i) IV of the storm; the time points are indicated by blue dashed lines in Fig. 1a. The diverging color bar is centered on the horizontal average to highlight the current anomalies. The domain is rotated counterclockwise 45° from the geographic coordinates referenced in Fig. 1b. Hence, winds initially from the east flow from the bottom right to the top left over the domain. As the eye of the storm passes during phase III [(d)–(f)], the source direction of the wind quickly rotates clockwise around the bottom of the domain to the left side, i.e., the southwest. The directions of the surface stress $\boldsymbol{\tau}$ and horizontally averaged shear vector at 5 m $\langle \partial \mathbf{u}_h/\partial z \rangle_{x,y}$ are indicated by the red and blue arrows, respectively, in the bottom-left corners. The roll coordinate charts used in Figs. 7 and 8 are overlaid in black.

at 5-m depth before 1500 UTC 27 August (see Watkins and Whitt 2020). Hence, the dominant large turbulent eddies are nearly isotropic with a characteristic scale similar to the OSBL depth during most of 27 August.

As the wind strengthens during the first half of 28 August (phase II), variance in both the horizontal currents and buoyancy increases at horizontal wavelengths $\lambda > 3D_{N^2}$ associated with large aspect ratios. In particular, horizontal kinetic energy at wavelengths $\lambda > 3D_{N^2}$ increases to more than half of the total horizontal kinetic energy at 5-m depth (Figs. 5a–c). And, the anomalous current speed in the streaks reaches a maximum characteristic magnitude of about 10 cm s^{-1}, which is roughly 10% of the mean speed, which grows from about 0.5 to 1.3 m s^{-1} during phase II. At the same time, the buoyancy variance at wavelengths $\lambda > 3D_{N^2}$ comes to represent more than 75% of the total variance shallower than 5-m depth (Figs. 5g–i). Hence, qualitatively similar streaks are visible in the plan views of temperature at 5 m, like the currents (cf. Figs. 4d and 6a), and the characteristic temperature anomalies in the streaks are a few tenths of a degree Celsius. The vertical kinetic energy also increases at wavelengths $\lambda > 3D_{N^2}$ during phase II (Figs. 5d–f). However, this large-scale vertical kinetic energy remains about two to three orders of magnitude weaker than the corresponding large-scale horizontal kinetic energy, as expected based on the aspect ratio of the flow structures. In addition, this large-scale vertical kinetic energy remains a small

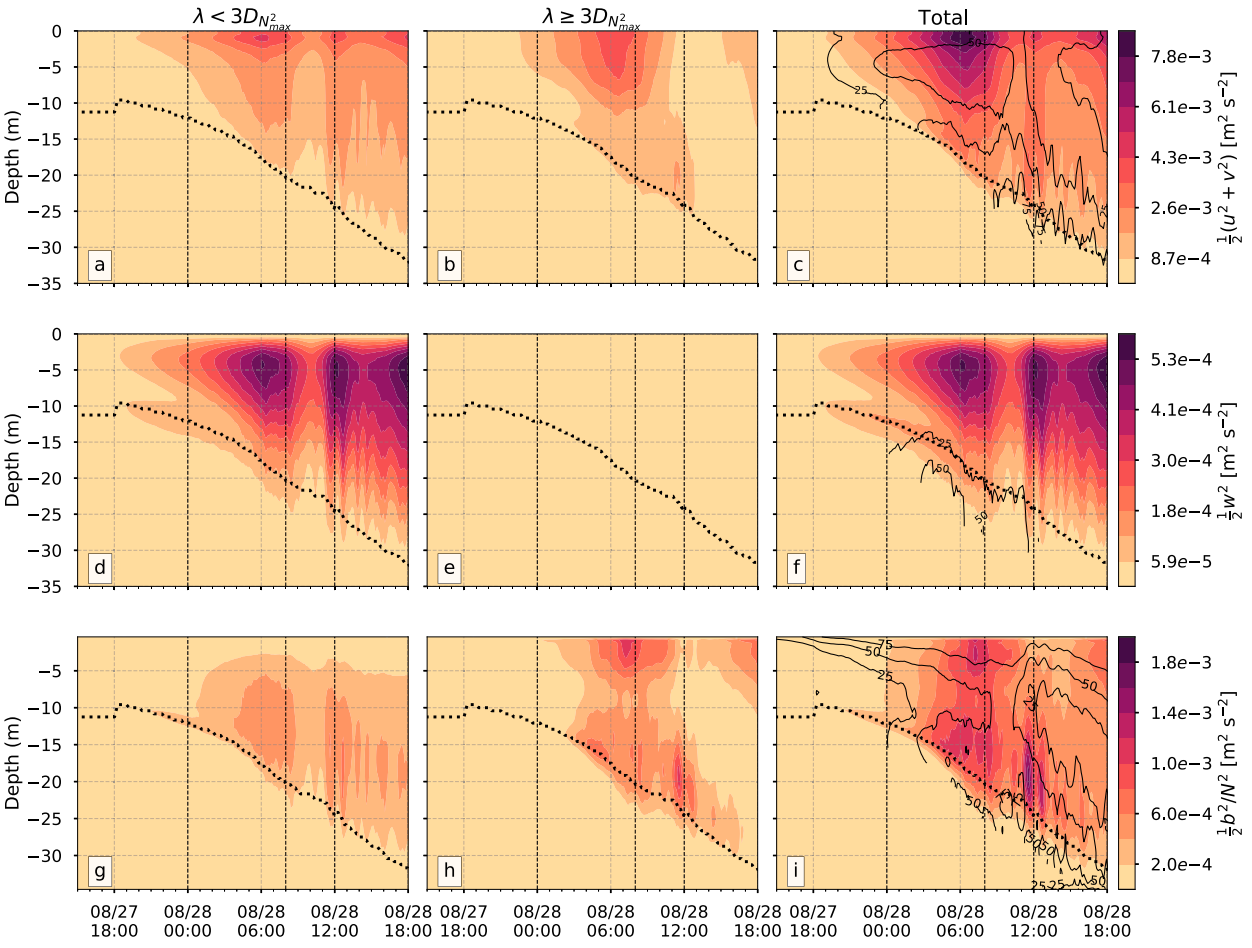

FIG. 5. (a)–(c) Horizontal and(d)–(f) vertical kinetic energy of the perturbations from the horizontally averaged flow, and (g)–(i) the buoyancy variance normalized by twice the mean vertical buoyancy gradient $\langle N^2 \rangle_{x,y}$. All three are decomposed using Fourier methods into wavelengths λ greater (center column) and smaller (left column) than 3 times D_{N^2}, the depth of maximum $\langle N^2 \rangle_{x,y}$, which is marked by a black dotted line. The black contours (every 25%) in the right column indicate the percentage of the variance accounted for by large scales (shown in the center column).

fraction of the total vertical kinetic energy, which remains dominated by wavelengths $\lambda < 3D_{N^2}$ typical of more isotropic OSBL turbulence.

Although the large-aspect-ratio streaks are prominent throughout phase II, when the wind is strong and persistently easterly, the streaks are not static. First, the streaks propagate at speeds comparable to the mean flow $\sim 1\,\mathrm{m\,s^{-1}}$, such that their characteristic time scale measured at a fixed position is of order 100 s. For example, at the beginning of phase III, the streaks propagate to the northwest in about the same direction as mean surface current, which points at an angle about 45° to the right of the wind (the mean flow will be discussed in later sections). However, in a reference frame following the mean flow in the upper 10 m, the streaks are nearly stationary and evolve with a much longer characteristic time scale more appropriately measured in hours than seconds, consistent with the time scale over which they initially emerge (see videos in the online supplemental material, https://doi.org/10.1175/JPO-D-20-0134.s1). Second, the dominant cross-streak wavelength λ_r increases with time during phase II, from approximately 100 to 300 m (Fig. 4). Perhaps not coincidentally, the depth D_{N^2} deepens from about 12 to 20 m at the same time (Fig. 5), such that the ratio λ_r/D_{N^2} remains in a narrower range of about 8–15. However, the orientation of the along-streak axis remains fairly consistent during phase II: it is rotated slightly clockwise ~10° from the wind vector (Fig. 4), which rotates slowly clockwise during phase II. As the wind rotates more quickly during phase III, the streaks also rotate more quickly clockwise with the wind. However, the amplitude of the current and temperature anomalies associated with the large-aspect-ratio streaks decays in both absolute terms and as a percentage of the total variance. The most obvious factor associated with the washing out of the streaks/rolls is the rate of rotation of the surface wind stress, which exceeds the local Coriolis frequency during eye passage in phase III. Thereafter, the streaks are not dominant features of the flow (Fig. 4), although the large-scale variance does increase toward the end of phase IV as the wind rotation slows and the direction stabilizes becoming consistently

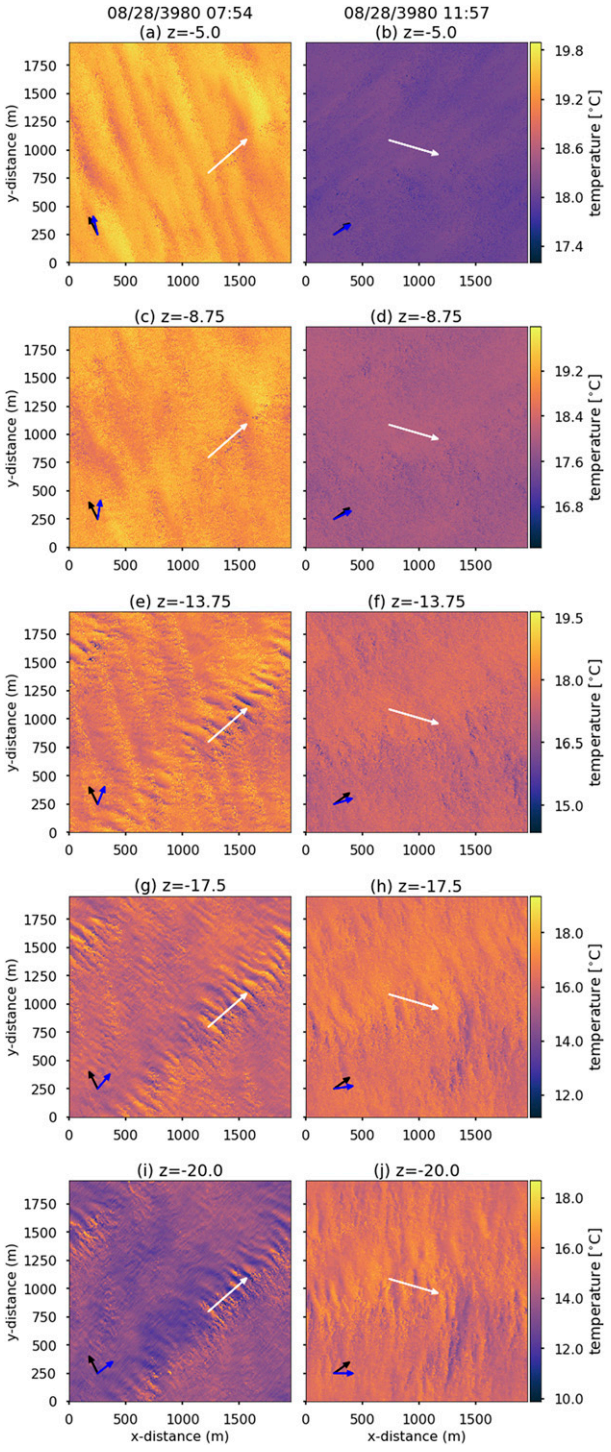

FIG. 6. Snapshots of temperature at both the (left) beginning and (right) end of phase III and at several depths (from top to bottom). The arrows in the bottom-left corner indicate the direction of the surface stress $\boldsymbol{\tau}$ (black) and the horizontally averaged shear vector $\langle \partial \mathbf{u}_h / \partial z \rangle_{x,y}$ at that depth. The white lines indicate the location of the vertical sections in Fig. 9.

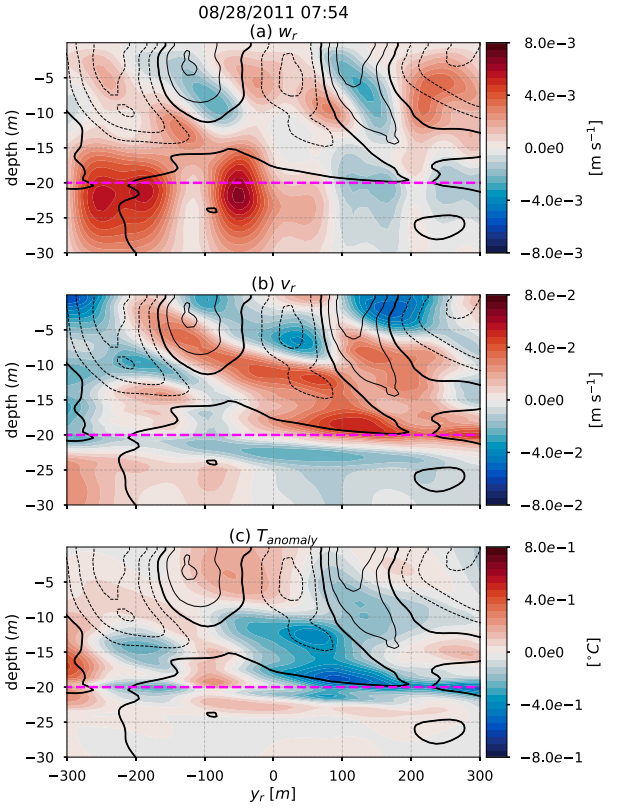

FIG. 7. (a) Vertical sections of vertical velocity, (b) cross-roll horizontal velocity, and (c) temperature, all of which are anomalies relative to the horizontal domain average. Overlaid is the along-roll streak velocity u_r (black contours every 4 cm s^{-1} have positive values marked by thin solid lines, negative values marked by thin dashed lines, and zero marked by the thick solid line) and D_{N^2} (magenta). The sections are along the cross-roll coordinate y_r shown in Fig. 4d, after smoothing with a 25-m Gaussian filter.

southwesterly to westerly (Figs. 4g–i and 5b,h), and the spinup time scale of the streaks in phase IV seems similar to their initial spinup time scale before the eye passes.

2) VERTICAL SECTIONS OF ROLLS/STREAKS IN ROLL COORDINATES

Vertical sections oriented perpendicular to the streak axis at the end of phase II highlight several key characteristics of the streaks/rolls and their impact on smaller-scale OSBL turbulence. We find that the cross-streak v_r and vertical w_r velocities form tilted rolls (Fig. 7) that are associated with the streaks u_r shown at 5-m depth in Fig. 4. The amplitude of the streaks/rolls decays rapidly with depth below 10 m, but their orientation in the horizontal plane does not rotate with depth despite substantial rotation of the mean shear vector (see Figs. 6 and 7). The simulated roll vertical velocity anomalies w_r have a characteristic scale of a few millimeters per second, and the corresponding cross-streak roll velocities v_r are a few centimeters per second, that is $v_r \sim 10 w_r$ consistent with the aspect ratio of about 10. The simulated horizontal cross-streak roll velocity v_r is about 3 times weaker than the along-roll streak velocity u_r.

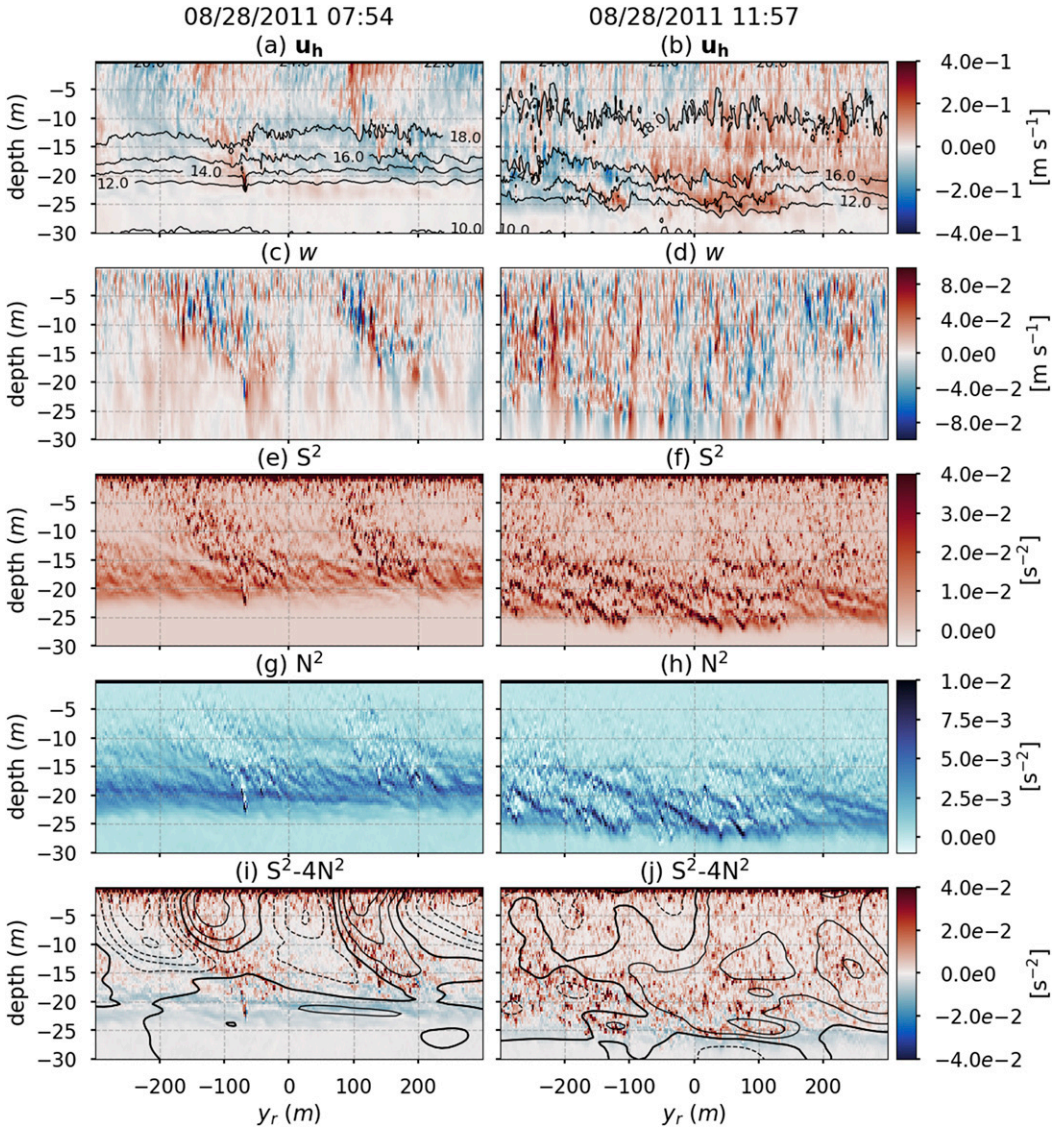

FIG. 8. As in Fig. 7, but without smoothing: (a),(b) anomaly in the horizontal speed $|\mathbf{u}_h|$, (c),(d) vertical velocity w, (e),(f) squared vertical shear of horizontal velocity S^2, (g),(h) stratification N^2, and (i),(j) reduced shear $S^2 - 4N^2$, just before (left) and just after (right) the eye. For reference, temperature contours are overlaid in (a) and (b) and smoothed u_r (also shown in Fig. 7) is overlaid in (i) and (j). The coordinate systems for before-eye and after-eye are plotted in Figs. 4d and 4f, respectively.

Thus, v_r stands out less prominently from other variability and appears less organized than u_r.

In addition, we find systematic correlations between the roll/streak variables, and thus an indication of net vertical transport by the streaks/rolls. In particular, the simulated streak velocity u_r is negatively correlated with w_r, although they are not perfectly aligned. The phase shift ϕ_r that minimizes the lagged correlation (to about -0.8) between $u_r(y_r)$ and $w_r(y_r + \phi_r)$ occurs at from $\phi_r \approx -20$ to -40 m or about $-0.1\lambda_r$. Conversely, temperature anomalies T_r are positively correlated with w_r, but the correlation coefficient is maximum (about $+0.6$) for a phase shift applied to w_r from $\phi_r \approx +10$ to $+40$ m or about $+0.1\lambda_r$. Thus, the results suggest that the roll-streak system may be associated with a downgradient momentum flux and positive shear production and upgradient buoyancy flux and positive buoyancy production. In a later section, we will separate by length scale and compare the turbulent vertical transport of momentum and buoyancy by these and all other structures and thereby explicitly quantify the impact of these structures on the evolution of the mean current and buoyancy profiles during the storm.

3) MODULATION OF SMALLER TURBULENCE

The vertical section plots in Fig. 8 show that the streaks modulate smaller-scale turbulence as well as the shear and stratification that influence the energetics of smaller scales. In particular, the region of strongest $\partial u_r/\partial z$, which is to the left (lower

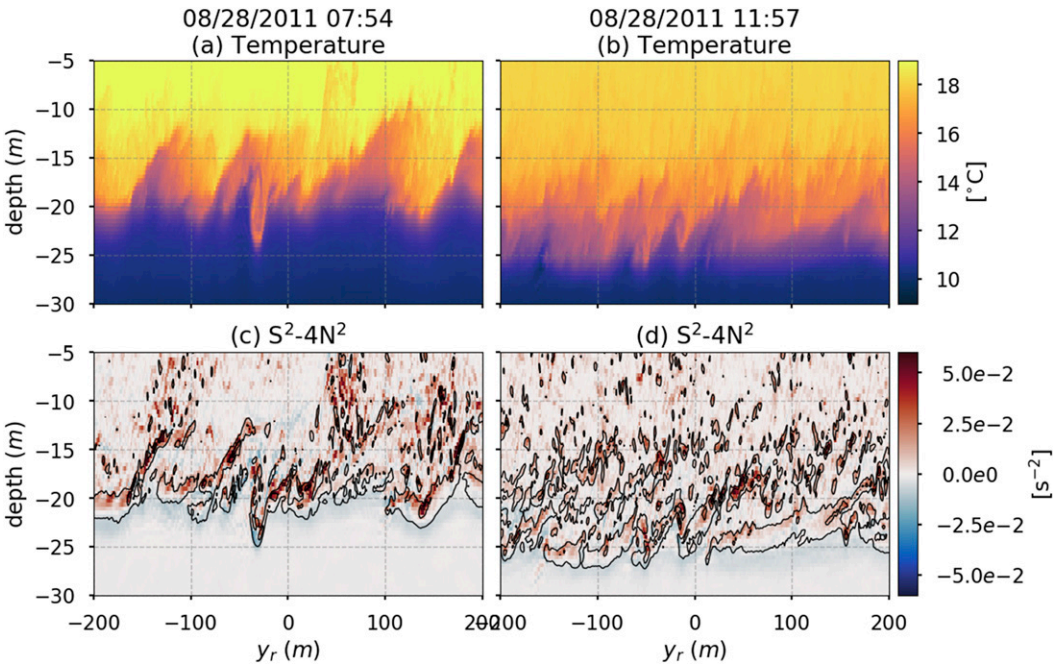

FIG. 9. (a),(b) Temperature and (c),(d) reduced shear with contours of vorticity (in x_r) overlaid in black along the white coordinate lines in Fig. 6.

y_r in roll coordinates) of and below positive streak anomalies ($u_r > 0$), is associated with a tongue of enhanced vertical velocity w variance, squared shear $S^2 = (\partial u/\partial z)^2 + (\partial v/\partial z)^2$ variance and stratification N^2 variance that extends downward and under the positive u_r anomaly, from the surface to the thermocline. In addition, the enhanced turbulence coincides with roll-scale downdrafts $w_r < 0$, which occur 20–40 m to the left of the streaks (toward lower y_r) and are correlated with cold temperature anomalies. This enhanced turbulence coincides with and is plausibly explained by strongly positive reduced shear, $S^2 - 4N^2 > 0$, in these regions (Fig. 8i), which is indicative of both a gradient Richardson number $\mathrm{Ri}_g = N^2/S^2 < 1/4$, hence the necessary conditions for instability are met (Miles 1961; Howard 1961; Hazel 1972), and substantial energy is available to the turbulence via shear production (Turner 1979; Rohr et al. 1988; Holt et al. 1992). Conversely, below the low-speed negative streak velocity anomalies ($u_r < 0$) turbulence is particularly weak and generally the reduced shear is negative and $\mathrm{Ri}_g \geq 1/4$. For comparison, a similar set of sections is shown after the eye passage in Fig. 8 in order to highlight the remarkable degree of periodicity imposed upon the turbulence by the streaks/rolls before the eye, under strong surface forcing.

b. Thermocline

Do the streaks and rolls discussed in the previous section, or large-aspect-ratio structures more generally, influence the entrainment of cold water from the thermocline and thereby the SST in the LES?

To begin addressing this question, we describe the characteristics of the dominant large structures in the turbulence near the thermocline, where the cold water enters the surface boundary layer. There, large scales $\lambda > 3D_{N^2}$ represent a majority of the horizontal kinetic energy and buoyancy variance between phases II and III (Fig. 5). In addition, plan views of temperature at different depths in Fig. 6 show that the characteristics of the large structures are qualitatively different at the thermocline compared to the surface-layer streaks/rolls. At the thermocline, the large-scale variance is dominated by smaller ~100-m-scale wave-like structures with crests and troughs perpendicular to the local shear vector $\partial\langle\mathbf{u}\rangle_{x,y}/\partial z$, which is rotated about 90° to the right of the wind stress. These wave-like features are reminiscent of organized KH billows (Fig. 9), so we refer to them as such before explicitly comparing to theory and prior observations in the discussion section below.

The significant spatial modulation of the KH billows is a feature of particular interest in such a large-aspect-ratio model domain. At the beginning of phase III, these features are organized into bands that are approximately parallel to the local shear vector, a few hundred meters wide, and spaced 1 km apart (Fig. 6g). Each band is associated with an undulation in the thermocline and horizontal velocity (e.g., it is warmer on the bottom-right and cooler on the top-left side of each band in Fig. 6g). These larger thermocline undulations are plausibly due to internal waves, but since these 1-km structures are not always this organized, we do not pursue a simple explanation for this kilometer-scale modulation. Nevertheless, the simulated axial coherence of the rolls (along lines of constant phase) is often at least several wavelengths, which is qualitatively consistent with existing albeit limited knowledge of axial coherence of KH-like billows observed in the atmosphere and laboratory (Thorpe 2002).

Although we do not explicitly plot the time evolution of the billows, we note that similar structures are prominent with

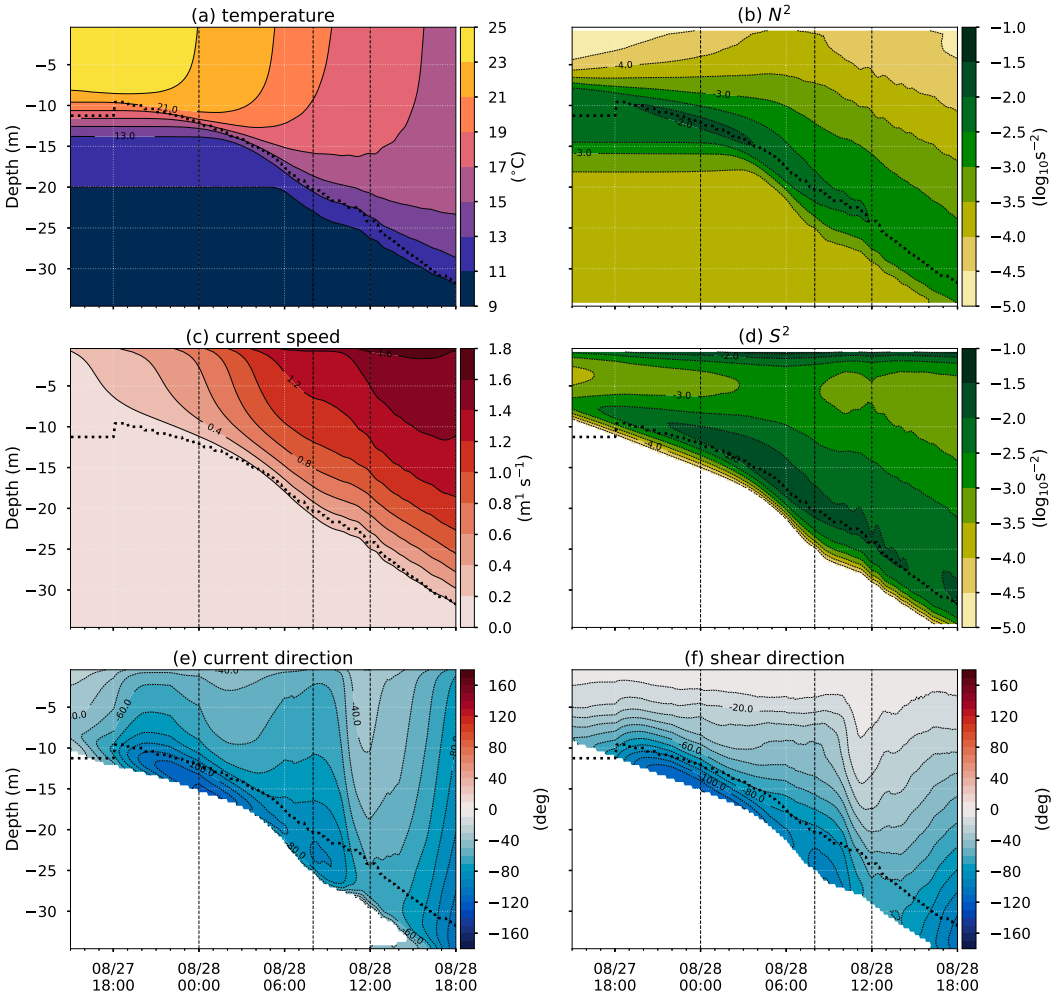

FIG. 10. (a) Mean vertical profiles of temperature, (b) vertical buoyancy gradient N^2, (c) horizontal current speed $|\mathbf{u}_h|$, (d) squared vertical shear of horizontal velocity S^2, (e) horizontal current direction, and (f) shear direction. Both of the angles in (e) and (f) indicate the direction the vector points and are given in degrees counterclockwise relative to the direction that the wind points. The angles are mostly negative and smaller than 90°, which indicates the current and shear vectors are to the right of the wind vector, as expected. Angles are only shown for speeds and shears greater than 10^{-3} m s^{-1} and s^{-1}, respectively. The dashed black line indicates the depth of maximum stratification D_{N^2}.

different degrees of organization at most times in phases II–IV (cf. Figs 9a and 9c with Figs. 9b and 9d; see also Fig. 6). In addition, the temporal evolution of the radially integrated horizontal wavenumber spectra of buoyancy variance and vertical kinetic energy at the time-dependent depth $z = -D_{N^2}$ both contain distinct local maxima at a wavelength λ that increases slowly from about 10–20 m at 1500 UTC 27 August to about 100 m at 0754 UTC 28 August (the beginning of phase III), during which time the depth D_{N^2} increases from about 10 to 20 m. Hence, unlike the surface streaks/rolls, which are more ephemeral and sensitive to the time-variability of the mean flow/forcing, the presence of organized wave-like or billow structures at the top of the thermocline is relatively robust to variations in the large scale conditions, although their precise spatial orientation and organization, characteristic scale, and magnitude varies.

4. Evolution of the mean profiles

The temporal evolution of the large-aspect-ratio structures is both dependent on and impacts the evolution of the mean profiles of momentum, temperature, salinity, and hence buoyancy. This section describes the temporal evolution of the horizontally averaged profiles of temperature, buoyancy, and momentum and then quantifies the net effects of the turbulence, including at large scales, on the mean profiles of momentum and buoyancy via vertical fluxes.

a. Mean profiles and comparisons to observations

In addition to generating the turbulence, the hurricane forcing also drives the evolution of the mean profiles, including the acceleration, deepening, and cooling of the OSBL (Figs. 10a,c).

For example, the forcing accelerates a sheared and surface-intensified mean current with speeds in excess of $1\,\mathrm{m\,s^{-1}}$ and shears in excess of $10^{-1}\,\mathrm{s^{-1}}$ (Figs. 10c,d). Even though the wind and currents are unsteady, the mean surface current vector points about 45° ± 20° to the right of the wind vector until late in phase IV (Fig. 10e), and the current vector rotates clockwise with increasing depth throughout phases I–IV, as in an idealized steady Ekman layer (Ekman 1905). In phase III, the wind rotates rapidly clockwise at an angular frequency of about $2f$ while fluctuating in speed as the eye passes (Fig. 1). As a result, the simulated angle between the ocean surface current vector and the wind vector is briefly reduced (Fig. 10e), as the wind rotates clockwise faster than the ocean surface current. In phase IV, the current angle decreases throughout the OSBL at a rate of about 15°–20° $\mathrm{h^{-1}}$ as the wind direction stabilizes, as in an idealized inertial oscillation (Ekman 1905; Pollard and Millard 1970).

The simulated OSBL depth begins deepening at the beginning of phase II and continues to deepen from about 10 to 30 m through the end of phase IV (Figs. 10a,b). In addition, the overall extent of the deepening as well as the time of most rapid deepening, which occurs just ahead of the eye passage at the beginning of phase III, are reasonably similar to the observations (Fig. 11). In addition, the deepening is reasonably consistent with the theoretical model of wind-driven mixed layer deepening without a bottom by Pollard et al. (1972), whose Eq. (6.1) suggests a poststorm mixed layer depth of 34 m based on just the initial stratification profile and the maximum wind stress.

As the OSBL deepens, the simulated SST cools by more than 4°C ahead of the eye during phase II and by more than 6°C by the end of phase IV, similar to observations (see Fig. 2 of Glenn et al. 2016). In addition, the most rapid SST cooling occurs before the eye passage and earlier than the most rapid OSBL deepening, as observed (Glenn et al. 2016).

Interestingly, the mean OSBL profiles remain stratified ($\langle N^2\rangle_{x,y} \sim 10^{-5}$–$10^{-4}\,\mathrm{s^{-2}}$) as well as sheared ($\langle S\rangle^2_{x,y} \sim 10^{-4}$–$10^{-3}\,\mathrm{s^{-2}}$) throughout the storm (Figs. 10b,d and 11). In addition, the mean shear and stratification within the OSBL evolve similarly so that the mean profiles contain a region of approximately marginal stability within the OSBL (e.g., Thorpe and Liu 2009; Smyth et al. 2019), where $\mathrm{Ri}_g = \langle N^2\rangle_{x,y}/\langle S\rangle^2_{x,y} \approx 1/4$ from about 5-m depth to about D_N^2 (Fig. 12). Above 5 m, Ri_g remains positive, but it is much less than 1/4 due to the strong surface layer shear near the air–sea interface. During the eye passage, the mean shear and stratification in the OSBL weaken, and Ri_g decreases suddenly from just above 1/4 to just below 1/4 (Fig. 12a). Thereafter, the Ri_g profile remains relatively consistent through the end of phase IV. A statistical measure of the spatial variability in Ri_g (Fig. 12) connects back to Fig. 8; the modulation of the reduced shear by the rolls occurs in conjunction with a reduced percentage (50%–75%) of the area from 5 m to the pycnocline that is locally unstable ($\mathrm{Ri}_g < 1/4$). In contrast, without the rolls and after the eye, more than 75% of the area is locally unstable through most of the OSBL.

The reasonably good comparison between the simulated and observed OSBL depth and SST response suggests that the simulated turbulent transport processes that drive these changes in the LES may be relevant to and important in the real ocean. However, although the evolution of the simulated surface current direction is similar to observations (in Fig. 2 of Glenn et al. 2016), and observed and simulated differences between top and bottom velocities are within about a factor of two, the magnitude of the simulated surface current is sometimes stronger than observed by more than a factor of 2. We attribute the stronger surface currents and weaker bottom currents in the LES to the absence of a pressure-gradient-driven flow opposed to the wind-driven surface current, which Glenn et al. (2016) found was significant via numerical simulations. In addition, it is notable that the observed mean stratification of the OSBL at the beginning of phase III is somewhat weaker than simulated ($\langle N^2\rangle_{x,y} \sim 10^{-5}$ versus $10^{-4}\,\mathrm{s^{-2}}$; cf. Fig. 11 and Fig. 10b). In this case, it is plausible that the relatively strong simulated stratification is attributable to missing surface gravity wave effects, but missing large-scale processes may also contribute to this stratification bias as well. We will return to a discussion of these missing processes below.

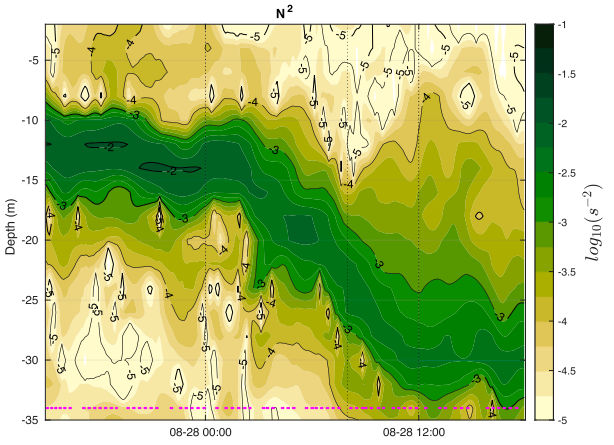

FIG. 11. Observed vertical buoyancy gradient N^2 in the region and time simulated by LES. Magenta dots at 34 m indicate the times of glider profiles sampled at 5-s resolution. The data have been linearly interpolated to a uniform 6 min × 2 m grid and smoothed with a forward-and-backward moving average with a 1-h (10-point) boxcar window and zero phase shift in an attempt to approximately mimic the spatial averaging that is applied in the analysis of the large-eddy simulation.

b. *Momentum flux*

In this idealized simulation, the horizontally averaged velocity vector $\langle \mathbf{u}_h\rangle_{x,y}$ only evolves due to the Coriolis force and the convergence of turbulent vertical fluxes of momentum, that is

$$\frac{\partial \langle \mathbf{u}_h\rangle_{x,y}}{\partial t} + \mathbf{f} \times \langle \mathbf{u}_h\rangle_{x,y} = \frac{\partial \mathbf{F}_m}{\partial z},$$

where $\mathbf{f} = (0, 0, f)$ is the traditional Coriolis frequency in vector form. This section complements the previous description of the evolution of $\langle \mathbf{u}_h\rangle_{x,y}$ with a description of the turbulent momentum flux, $\mathbf{F}_m = \langle \nu_{\mathrm{SGS}} \partial \mathbf{u}_h/\partial z - w\mathbf{u}_h\rangle_{x,y}$, which is dominated

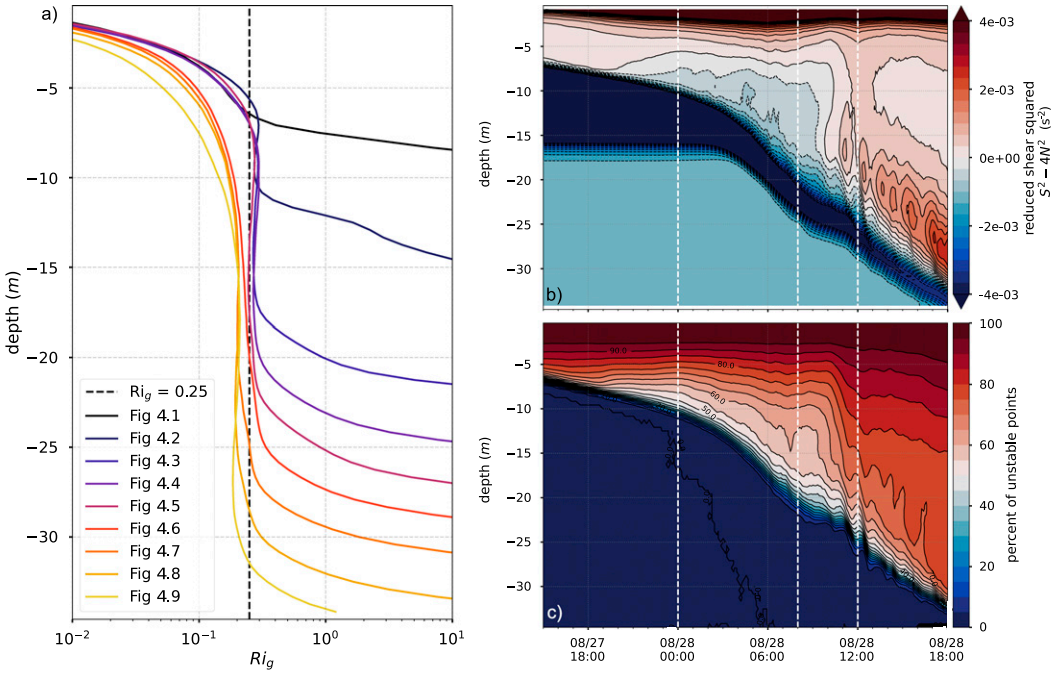

FIG. 12. Profiles of (a) the gradient Richardson number $\mathrm{Ri}_g = N^2/S^2$ and (b) the reduced shear $S^2 - 4N^2$ (s^{-2}) associated with the mean velocity and buoyancy profiles. (c) The percent of all points where the reduced shear is positive at each depth. The profiles all cluster into two regimes that separate by time: before and after eye passage, which occurs at about 0900 UTC 28 Aug (see Figs. 1 and 2).

by the resolved flux $-\langle w\mathbf{u}_h\rangle_{x,y}$ throughout most of the OSBL.[2] We characterize this flux in terms of its magnitude and direction, and we decompose it into two scales: smaller and larger than $3D_{N^2}$ (with subgrid-scale fluxes lumped with small scales). In addition, we quantify the effective turbulent viscosity profile, which we define by

$$\nu_t = \frac{\mathbf{F}_m \cdot \partial\langle\mathbf{u}_h\rangle_{x,y}/\partial z}{|\partial\langle\mathbf{u}_h\rangle_{x,y}/\partial z|^2}. \tag{1}$$

This definition of the scalar turbulent viscosity ν_t does not account for the nonlocal component of $\mathbf{F}_m$, i.e., the component of $\mathbf{F}_m$ that is perpendicular to $\partial\langle\mathbf{u}_h\rangle_{x,y}/\partial z$ (e.g., Large et al. 2019), which modifies ν_t by 3% or less in this scenario. Nevertheless, we still quantify the nonlocal component of $\mathbf{F}_m$ via the angle Ω between $\mathbf{F}_m$ and $\partial\langle\mathbf{u}_h\rangle_{x,y}/\partial z$ (e.g., Large et al. 2019), since the magnitude of the nonlocal flux is as large as 25% of $|\mathbf{F}_m|$ and thus may significantly influence the evolution of $\langle\mathbf{u}\rangle_{x,y}$ but is not accounted for in some OSBL mixing parameterizations (e.g., Large et al. 1994).

In this strongly forced regime, the magnitude of the shear is always positive, and the evolution of the momentum flux is controlled by the surface stress (see Fig. 1), which sets the surface value of $\mathbf{F}_m$. We also find that $|\mathbf{F}_m|$ decays approximately linearly with depth from the surface to about $z = -D_{N^2}$ while entrainment is occurring during phases II–IV (Figs. 13 and 14). Deviations from a linear $\mathbf{F}_m(z)$ profile do occur, but they have a magnitude of only about $0.2u_*^2$ where the friction velocity $u_* = \sqrt{|\boldsymbol{\tau}|/\rho_0}$. In addition, the turbulent viscosity collapses to a virtually time-independent vertical profile when ν_t is made dimensionless by dividing by $ku_*D_{N^2}$ and the depth z is divided by D_{N^2} (e.g., Large et al. 1994).

The decomposition of $\mathbf{F}_m$ into large and small scales (Fig. 14) shows that the flux is dominated by small wavelengths $\lambda < 3D_{N^2}$ at all depths and times. However, larger scales are nonnegligible, particularly during phase II and the beginning of phase III in the top 10 m, where the streaks and rolls are prominent and large scales account for about 10%–20% of the total flux. Just above the thermocline ($z = -D_{N^2}$), the large scale contribution to the flux is more intermittent and relatively weaker; it only just reaches 10% of the total flux at the beginning of phase III.

After the eye passage during phases III–IV, the acceleration of the OSBL continues, but the large-scale contribution to the flux is substantially smaller in percentage terms than before the eye. In addition, $|\mathbf{F}_m|$ briefly exhibits a relatively large ($\sim 0.2u_*^2$) positive deviation from the linear profile in the middle of the

[2] The subgrid-scale terms are only significant within a few meters of the surface and in the thermocline, hence the mean response and large-scale structures are expected to be fairly insensitive to refining the grid resolution (e.g., Whitt et al. 2019). Although it is prohibitively costly to significantly increase the resolution and test this in the large domain considered here, we confirmed this expectation by refining the grid resolution by a factor of 2 in all dimensions in a smaller domain.

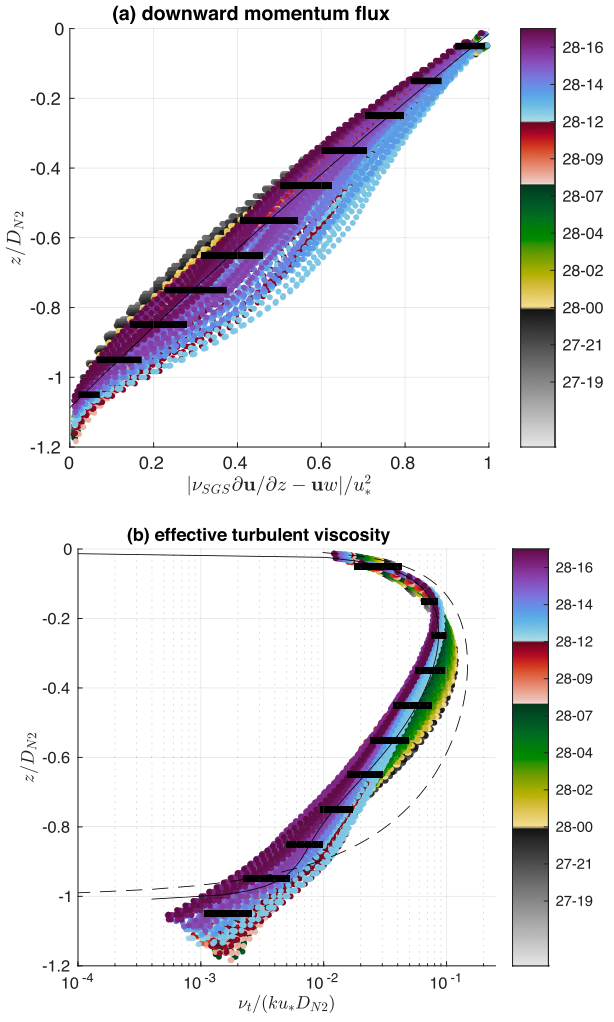

FIG. 13. (a) The momentum flux scaled by the friction velocity u_* decays nearly linearly with decreasing z/D_{N^2} at all times when entrainment is occurring (color bar, day-hour). The correlation coefficient between z/D_{N^2} and $|\mathbf{F}_m|$, where $\mathbf{F}_m = \langle \nu_{SGS}\partial\mathbf{u}/\partial z - \mathbf{u}w\rangle_{x,y}$, is 0.98. The best fit quadratic (for $z/D_{N^2} > -1.2$) has coefficients −0.11, 1.18, and 1.09 (beginning with the highest-order term). (b) The effective turbulent viscosity, $\nu_t = \mathbf{F}_m \cdot \langle \partial\mathbf{u}_h/\partial z\rangle_{x,y}/|\langle \partial\mathbf{u}_h/\partial z\rangle_{x,y}|^2$, collapses when scaled by $ku_*D_{N^2}$, where $k = 0.4$ is the von Kármán constant. The best-fit quadratic (for $z/D_{N^2} > -1$) has coefficients −1.28, 3.41, −3.09, 0.97, and −0.01 and explains 88% of the variance for $z/D_{N^2} > -1$. Standard deviations in 11 bins are indicated by thick black bars. The dashed line in (b) is the empirical function $-z/D_{N^2}(1 + z/D_{N^2})^2$; a similar function is used in the *K*-profile parameterization scheme of Large et al. (1994).

OSBL (at about 1200 UTC 28 August, perhaps because the wind is particularly strong and well aligned with the shear, as shown in Fig. 10f) but thereafter returns to a nearly linear profile that persists through the end of phase IV.

The angle Ω between the momentum flux and the mean shear vector is also plotted as a function of time and scale in Fig. 14. In both the total and small-scale part of $\mathbf{F}_m$, Ω is small but nonnegligible, reaching maxima of about 15° and 10°, respectively, between about 5–10 m at the end of phase II (for reference, this implies that the nonlocal component of $\mathbf{F}_m$ is 17%–26% of the magnitude $|\mathbf{F}_m|$). With respect to the total and small-scale fluxes, Ω is very slightly negative at the surface, but positive throughout most of the OSBL during phase II. That is, the corresponding $\mathbf{F}_m$ vector is rotated counterclockwise relative to the local shear $\partial\langle\mathbf{u}_h\rangle_{x,y}/\partial z$ and toward the wind stress vector $\boldsymbol{\tau}$ in most of the OSBL.

It may be noted that the total and small-scale nonlocal fluxes are correlated in time with large-scale nonlocal fluxes, which are associated with much greater Ω, particularly in the middle of the OSBL. Hence, we consider the hypothesis that the nonlocal momentum flux, i.e., the occurrence of $\Omega \neq 0°$ in Figs. 14d–f, is due to the presence and modulating effects of the large-scale rolls/streaks. The evidence in support of this hypothesis is as follows. First, the magnitude ($w_r u_r \sim 10^{-4}\,\mathrm{m^2\,s^{-2}}$), depth range (top 10 m), and angle Ω of the large-scale fluxes (Figs. 14c,f) are consistent with the roll structures described in section 3 (Fig. 7). In particular, Ω (Fig. 14f) is slightly negative near the surface, where the streaks are rotated to the right of the wind stress and local shear, but Ω increases with depth as the mean shear vector rotates clockwise but the rolls and streaks remain at a fixed angle (see Figs. 6 and 7). Second, the temporal evolution of the nonlocal fluxes at small scales (Fig. 14e) is similar to the temporal evolution of the streaks as well as the associated large-scale fluxes (cf. to Figs. 5b,h and 14c). In particular, both the magnitude of the large-scale streaks/rolls and the small-scale nonlocal fluxes are largest during phase II and abruptly transition to much smaller values as the eye passes. Further, the small-scale turbulence is modulated by and more intense below the streaks ($u_r > 0$) (Figs. 8c,e,i), where the large-scale shear vector is rotated counterclockwise relative to the mean shear vector. To the extent this relationship is significant and strong, a positive Ω at small scales (Fig. 14e) is expected at the base of the streaks while they are present. Together, all of this evidence suggests that the nonlocal momentum flux, at large and small scales, is directly or indirectly due to the presence of the large-aspect-ratio streaks and rolls. In addition, explicit models of these large-aspect-ratio structures may be necessary to model nonlocal fluxes in OSBL mixing parameterizations.

Thus, we conclude that the large-aspect-ratio structures fundamentally alter the direction and magnitude of the momentum flux and thus the evolution of the mean momentum profile in this scenario, but the magnitudes of these modifications are relatively small (~10%) compared to the fraction of turbulent kinetic energy in these large scales (>50%).

c. *Entrainment and buoyancy flux*

The rapid SST cooling and the associated impacts on the hurricane are driven by entrainment and the downward turbulent buoyancy flux as the OSBL penetrates into the cold thermocline. In particular, since the OSBL is approximately mixed and the mean buoyancy profile is highly correlated with the mean temperature profile (Fig. 3), the evolution of the SST is governed by the evolution of the buoyancy averaged over $z > -D_{N^2}$ (Stevenson and Niiler 1983), which evolves according to

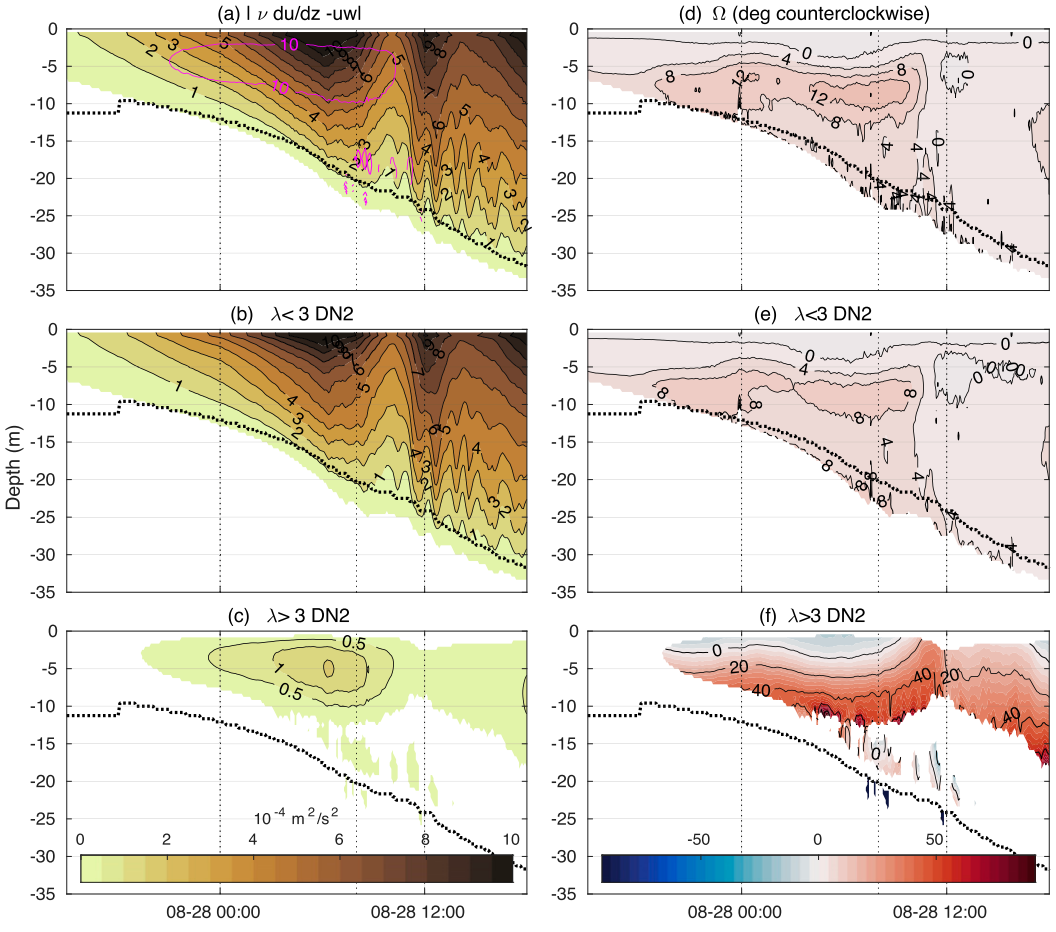

FIG. 14. The (left) magnitude and (right) direction of the downward vertical momentum flux vector $\mathbf{F}_m = \langle \nu_{SGS} \partial \mathbf{u}_h / \partial z - w \mathbf{u}_h \rangle_{x,y}$. The direction is given relative to the local mean shear vector $\langle \partial \mathbf{u}_h(z,t)/\partial z \rangle_{x,y}$, which is shown in Fig. 10f. (a) The total flux is also decomposed, via Fourier transforms, into (b) small scales, that is, horizontal wavelengths $\lambda < 3D_{N^2}$ including subgrid scales, and (c) large scales, that is, horizontal wavelengths $\lambda > 3D_{N^2}$. For reference, the black dotted line indicates D_{N^2}. The magenta contours in (a), marked every 10%, indicate the percentage of the total flux that is attributable to large scales.

$$\frac{\partial}{\partial t}\left(\langle b \rangle_{x,y,D_{N^2}}\right) = \frac{F_b(z=0) - F_b(z=-D_{N^2})}{D_{N^2}} - \frac{\Delta b}{D_{N^2}} \frac{\partial D_{N^2}}{\partial t}, \quad (2)$$

where $\Delta b = \langle b \rangle_{x,y,z>-D_{N^2}} - \langle b \rangle_{x,y}(z=-D_{N^2})$ and

$$F_b = \langle \kappa_{SGS} \partial b/\partial z - wb \rangle_{x,y}.$$

In addition, the evolution of the mean buoyancy profile is governed by

$$\frac{\partial \langle b \rangle_{x,y}}{\partial t} = \frac{\partial F_b}{\partial z}.$$

Therefore, this section quantifies F_b and the related entrainment flux $F_e = -\Delta b \partial D_{N^2}/\partial t$ in order to evaluate the impact of the storm-driven OSBL turbulence, and the large-aspect-ratio structures in particular, on the evolution of the mean buoyancy and stratification profiles, entrainment, and SST cooling.

First, it is notable that the buoyancy flux profile F_b collapses when divided by F_e (Fig. 15c). The maximum of F_b is found at $z \approx -3D_{N^2}/4$ throughout the storm, and the magnitude of this maximum is approximately equal to $3F_e/4$ on average (Figs. 15a,c). About 80% of the temporal variance in the maximum of F_b (Fig. 15a) can be explained by variations in the rate of entrainment F_e. In addition, a similarly large fraction of the temporal variance in F_e (and F_b) can be explained by the rate of working on the surface current by the wind stress $\boldsymbol{\tau} \cdot \mathbf{u}$ $(z = 0)$ divided by D_{N^2} (Fig. 16).[3] During the end of phase III and the beginning of phase IV, when the angle between the wind and the current is relatively small (Fig. 10e), the dot product in $\boldsymbol{\tau} \cdot \mathbf{u}$ $(z = 0)$ is particularly crucial; it is only at this time that the conventional friction

[3] As Bill Large suggested to us, the shear production averaged above D_{N^2} explains F_e about as well as the wind work. Motivated by that suggestion, we also find that the surface stress dotted into the average shear above D_{N^2}, i.e., $\tau \cdot \langle \partial \mathbf{u}_h/\partial z \rangle_{x,y,z>-D_{N^2}}$ explains the entrainment about equally well too.

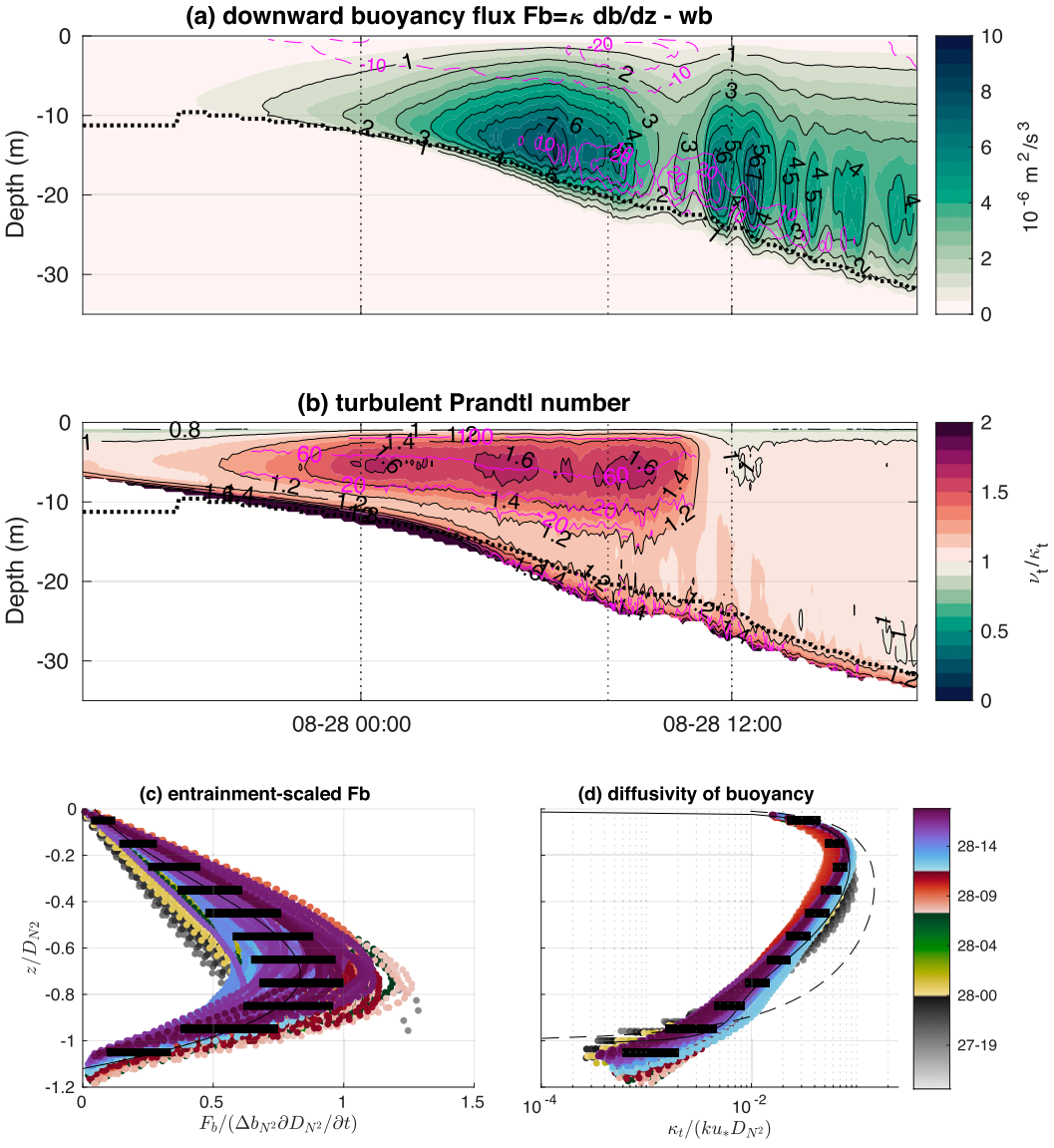

FIG. 15. (a) The vertical buoyancy flux $F_b = \langle \kappa_{SGS} \partial b/\partial z - bw \rangle_{x,y}$, which is collapsed in (c) by dividing by the entrainment buoyancy flux $F_e = \Delta b \partial D_{N^2}/\partial t$, where Δb is the difference between the depth-averaged buoyancy above D_{N^2} and the buoyancy at D_{N^2}. The color bar in (c) and (d) indicates the time (day-hour). The best-fit cubic in (c) (solid black line), which explains 86% of the variance of F_b, has coefficients −3.07, 2.82, 0.65, and 0.05 (from highest to lowest order). The turbulent diffusivity profile $\kappa_t = F_b/N^2$ in (d) is very similar to the turbulent viscosity profile ν_t (plotted in Fig. 13b), but the turbulent Prandtl number $\mathrm{Pr}_t = \nu_t/\kappa_t$ systematically differs from 1, as shown in (b). For reference, magenta contours in (a) and (b) quantify the percentage of F_b and $\mathrm{Pr}_t - 1 > 0.2$, respectively, that are attributable to fluctuations with wavelengths greater than $3D_{N^2}$. In both (c) and (d), horizontal black bars indicate standard deviations in 11 depth bins. For reference, the depth D_{N^2} (dotted black) is overlaid in (a) and (b), and the solid black and dashed black curves in (d) are the same dimensionless viscosity model profiles as in Fig. 13b.

velocity scaling u_*^3/D_{N^2}, which works reasonably well in phases I–III and late in phase IV, is too weak (Fig. 16). Hence, the rapid ahead-of-eye SST cooling in the LES is due to two factors: 1) the relatively large injection of kinetic energy from the wind to the OSBL ahead of the eye passage in phase II (due to the large friction velocity; see Fig. 16), and 2) the relatively small D_{N^2} at that time. The latter effect is quadratically important, since $\partial \langle b \rangle_{x,y,D_{N^2}}/\partial t \sim F_e/D_{N^2} \sim \boldsymbol{\tau} \cdot \mathbf{u}(z = 0)/D_{N^2}^2$ [see Eq. (2)].

Second, it is notable that F_b has a relatively large magnitude in the OSBL throughout the storm. Specifically, the flux Richardson number (Osborn 1980)

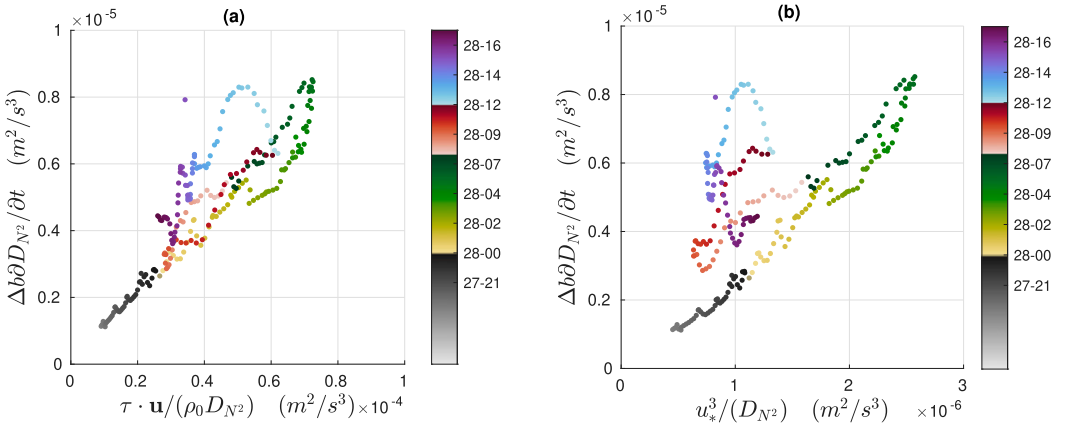

FIG. 16. The relationship between the entrainment flux F_e and the rate of working on the surface current by (a) the wind stress ($r^2 = 0.75$, linear regression slope = 0.1) and (b) the friction velocity u_*^3 ($r^2 = 0.37$, linear regression slope = 2.0) during entrainment. The color bar indicates the time (day-hour).

$$\mathrm{Ri}_f = \frac{F_b}{\mathbf{F}_m \cdot \partial \langle \mathbf{u} \rangle_{x,y}/\partial z} \sim 0.1$$

throughout most of the OSBL. In particular, $\mathrm{Ri}_f \sim \mathrm{Ri}_g$ (Fig. 17), and hence the buoyancy flux is 10% or more of the shear production where $\mathrm{Ri}_g \gtrsim 0.1$. That is, the strong wind makes buoyancy relevant to the turbulence energetics via entrainment, even though the Monin–Obukhov length is at least an order of magnitude greater than D_{N^2}, and the surface buoyancy flux $F_b(z = 0) \ll \max_z(F_b)$ is relatively small (cf. Figs. 1c and 15a).

Third, F_b is composed mostly of small scales $\lambda < 3D_{N^2}$, but large scales $\lambda > 3D_{N^2}$ make a nonnegligible contribution to the total F_b (similar to $\mathbf{F}_m$) (cf. Figs. 15a and 14). Specifically, the large scales are responsible for a countergradient flux $F_b < 0$, which is equal in magnitude to 10%–30% of the total $|F_b|$ in the upper 5–10 m during phases II–III. And, large scales are responsible for a downgradient flux equal to 10%–20% of the total F_b just above the thermocline during phases II–IV (Fig. 15a). Plots of F_b as a function of horizontal wavelength and depth at the beginning and end of phase III in Figs. 18a and 18b highlight the spatial and spectral localization of the large-scale buoyancy fluxes as well as the abrupt decay of the near-surface streaks/rolls and the associated large-scale fluxes during phase III. These spectra also provide explicit quantitative support for the hypothesis implicitly espoused in section 3: that there are a small number of distinct structures that dominate the large-scale dynamics, rather than a turbulent continuum at large scales. That is, although a scale separation is an imperfect way of separating the large-aspect-ratio rolls and billows from the turbulent continuum, the scale separation effectively achieves that end in this case. Most of the large-scale contribution to F_b can essentially be attributed to either the near-surface rolls/streaks in the top 10 m or the KH-like billows just above D_{N^2}, as described in section 3. Nevertheless, a cautious interpretation is still warranted: some of the flux associated with the KH-like billows is apparently categorized as small scale (to the right of the red line in Fig. 18), and some of the large-scale flux is evidently not associated with the dominant large structures described in section 3.

Finally, it is notable that although the buoyancy flux varies systematically with the momentum flux such that the turbulent Prandtl number $\mathrm{Pr}_t = \nu_t/\kappa_t$ is always near 1 [ν_t and κ_t are defined as in Eq. (1)], there are also persistent deviations $\mathrm{Pr}_t > 1$ (Figs. 15b and 17). In addition, these positive deviations in Pr_t coincide with and are partially attributable to: 1) the presence of the Ekman-layer rolls, which increase the overall Pr_t by reducing κ_t and increasing ν_t (see Figs. 18a,c,e; cf. Figs. 17a,b), 2) the increased mean-profile Ri_g, which is associated with higher $\mathrm{Pr}_t = \mathrm{Ri}_g/\mathrm{Ri}_f$ and lower Ri_f relative to Ri_g for $\mathrm{Ri}_g \approx 0.25$ (see Figs. 12 and 17), and 3) the nonlocal momentum flux during phase II, which does not directly modify Pr_t more than a few percent but is thought to be another consequence of the Ekman-layer rolls (Fig. 14). Conversely, the KH-like structures do not directly increase Pr_t. Just above the thermocline, the scale-dependent Prandtl number is generally positive but less than 1/2 over the depth range and wavelengths characteristic of the KH-like billows, which are more effective at transporting buoyancy than momentum and thus directly contribute to lowering Pr_t and increasing Ri_f (ignoring the indirect effects of these structures on Pr_t via smaller wavelengths; see Fig. 18).

In summary, although entrainment and SST cooling is controlled to a first approximation by the mean dynamics [i.e., it is a response to the wind work on the mean flow, as in Pollard et al. (1972)], the large-aspect-ratio structures contribute ~10% to the vertical buoyancy flux and thus may modify the SST response by ~10% (i.e., a few tenths or possibly even a whole degree Celsius).

5. Discussion

Before concluding, we briefly compare our simulation study with a few prior observational studies focused on the instabilities of both the Ekman boundary layer and stratified shear layers, which are thought to be relevant to the near-surface streaks/rolls and the KH-like billows near the thermocline,

respectively. In the second section below, we explicitly discuss the possible significance and implications of two omitted processes, surface gravity waves and larger-scale ocean dynamics.

a. Comparisons with prior studies

1) EKMAN LAYER ROLLS

Perhaps the most plausible dynamical causes of the simulated near-surface streaks and rolls are the linear instabilities of the Ekman layer (Kaylor and Faller 1972; Brown 1972; Asai and Nakasuji 1973; Lemone 1973; Duncombe 2017; Skyllingstad et al. 2017). These instabilities produce helical rolls/streaks approximately aligned with the geostrophic wind in the atmosphere and surface stress in the ocean (often tilted at some small angle ~10° relative to the wind or stress) that are qualitatively similar to the near-surface streaks and rolls described in section 3 [e.g., compare Fig. 7 with Fig. 4a of Lemone (1973)]. In particular, the roll circulation (v_r, w_r) as shown in Fig. 7 is typically surface intensified and inclined in the cross-roll-vertical plane. In addition, the cross-roll wavelength $\lambda_r \sim 10D_{\rm Ek}$, where $D_{\rm Ek} = \sqrt{2\nu_t/f} \approx 15$ to 30 m and $\nu_t \sim 0.1ku_*D_{N^2}$ as in Fig. 13b (e.g., Lemone 1973; Asai and Nakasuji 1973; Sous et al. 2013).

There are also some notable similarities between the simulated streaks/rolls and observations of such features in the ABL, as reported by Lemone (1973, 1976). In both this LES and the ABL observations, the roll-streak system is associated with a downgradient momentum flux and positive shear production and upgradient buoyancy flux and positive buoyancy production. Further, the simulated roll-scale modulation of small-scale turbulence, which is enhanced in roll downdrafts $w_r < 0$ that correspond with cold temperature anomalies, is qualitatively analogous to the ABL observations, in which turbulence is enhanced in roll updrafts that correspond with warm temperature anomalies.

There are also some notable differences between our simulated rolls/streaks and those observed by Lemone (1973, 1976). For example, the cross-roll velocity v_r was stronger and more organized than the streak velocity u_r in their ABL observations, whereas the streak velocity u_r is stronger and more organized than the cross-roll velocity v_r in these ocean LES. Second, Lemone (1973) only observed the regime where $D_{\rm Ek} \ll D_{N^2}$ and thus found that $\lambda_r \sim D_{N^2}$, whereas in the LES $\lambda_r \sim 10D_{N^2}$ and w_r is thus much weaker than v_r, unlike their ABL observations. Further, Lemone (1976) finds that the observed modulation of smaller-scale turbulence in the ABL is explained by roll-scale vertical transport of small-scale turbulence via w_r in the absence of strong coherent streaks u_r. Although vertical transport of turbulence plausibly contributes to the observed roll-scale modulation of turbulence in the LES, the strong simulated streaks and the close relationship between positive reduced shear (below $u_r > 0$) and enhanced turbulence in the LES suggests that the strong streaks also contribute energy to the smaller-scale turbulence via shear production and thereby the overall roll-scale modulation of small-scale turbulence in the LES.

The favorable comparisons between the LES and ABL observations is encouraging, but the lack of direct observations of such rolls in the OSBL under Hurricane Irene means the realism of the simulated turbulence cannot be verified observationally. Direct comparisons to oceanic observations of the turbulence derived from the glider are not pursued here as the observations required to estimate vertical velocity variance (e.g., Merckelbach et al. 2019) were unavailable since the glider was lost before recovery. Temperature, conductivity, and pressure data were recorded at 5-s intervals and sent via the Iridium connections approximately every 3 h or every 5–7

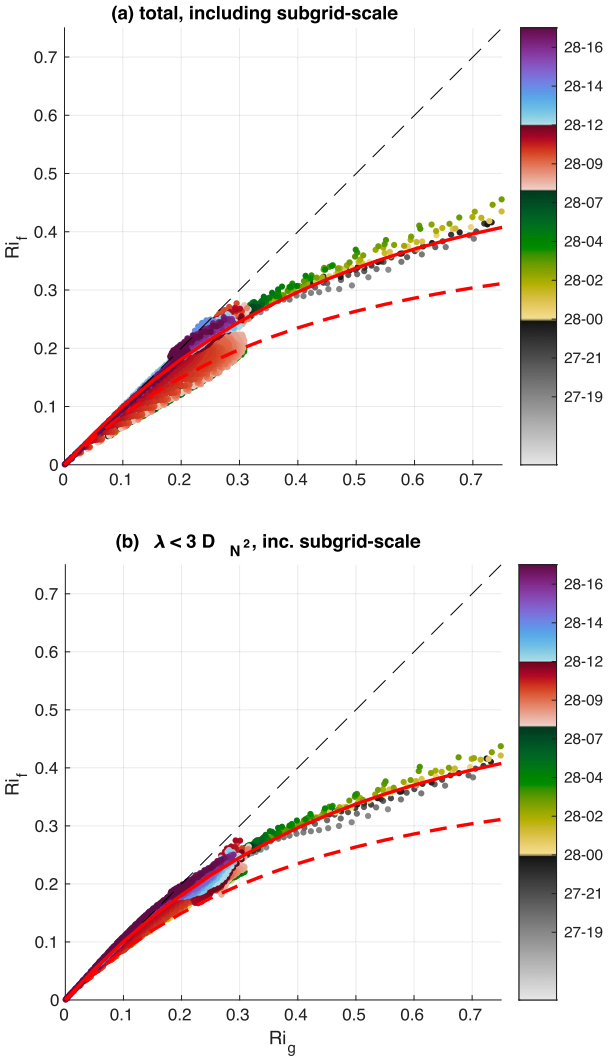

FIG. 17. The relationship between the gradient Richardson number Ri_g and flux Richardson number Ri_f above the depth of maximum stratification D_{N^2} where Ri_f is either as simulated (dots) or determined from Ri_g via $\mathrm{Ri}_f = 0.5(1 - e^{-2.25\mathrm{Ri}_g})$ (the solid red curve), which explains 93% and 98% of the variance in (a) and (b), respectively (e.g., Venayagamoorthy and Koseff 2016). In (a), the simulated Ri_f is calculated using the total buoyancy and momentum fluxes (including the subgrid scales), whereas in (b) the simulated Ri_f is calculated using only the wavelengths $\lambda < 3D_{N^2}$ (and the subgrid scales). The dashed red curve is a parameterization based on the ABL measurements (Anderson 2009), which parameterizes the subgrid-scale Ri_f in the LES (see section 2). The color bar indicates the time (day-hour).

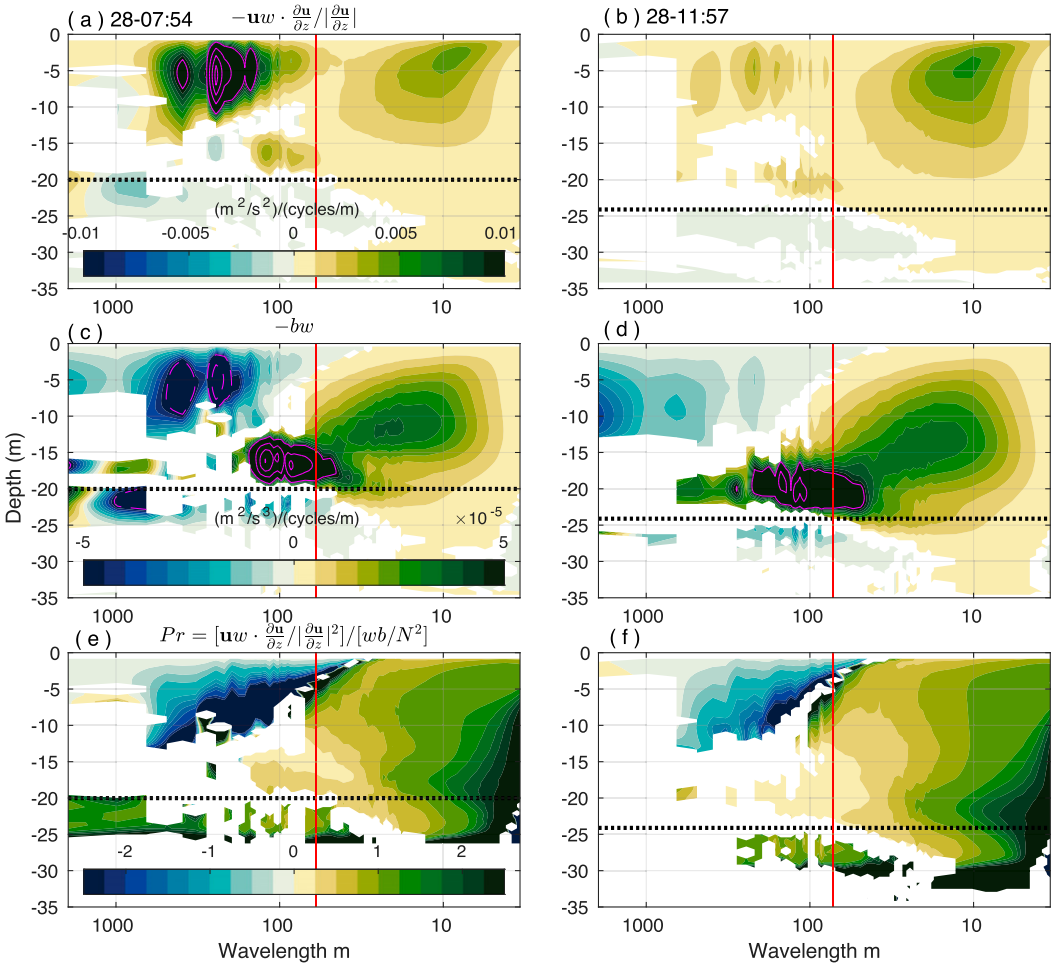

FIG. 18. Momentum and buoyancy flux cospectra at each depth averaged over 2-h windows centered at the (left) beginning and (right) end of phase III (see Fig. 1). Magenta contours, which are given every 0.01 $m^2 s^{-2}$ (cycles per meter) in (a) and 0.000 05 $m^2 s^{-3}$ (cycles per meter) in (c) and (d), respectively, highlight regions and wavelengths of particularly strong covariance before and after eye passage. Areas where the covariance is not significantly different from zero are blanked. The dotted black horizontal lines indicate the depth D_{N^2}, and the vertical red lines indicate the wavelength $3D_{N^2}$. The ratio of the relevant covariances, i.e., the flux Richardson number Ri_f, is decomposed by horizontal wavelength λ and written as a turbulent Prandtl number $\mathrm{Pr} = \mathrm{Ri}_g/\mathrm{Ri}_f$ in (e) and (f), where $\mathrm{Ri}_g = \langle N^2 \rangle_{x,y} / \langle S \rangle^2_{x,y}$ is the gradient Richardson number of the horizontally averaged velocity and density profiles.

downcast–upcast cycles. In summary, we lack the spatiotemporal resolution to isolate the roll structures or other features of interest in the turbulence that would allow for a useful direct comparison between the simulated and observed turbulence under Hurricane Irene.

Nevertheless, there are numerous observational indications of helical rolls such as those simulated in the LES in the ocean [going back to, e.g., Langmuir (1938); see section 1]. And some of these observed OSBL rolls/streaks have been simulated in LES and are qualitatively insensitive to the effects of surface gravity waves, which are omitted here (see Sundermeyer et al. 2014). Thus, the simulated large-aspect-ratio structures are plausibly realistic, even without surface gravity waves or larger-scale processes. However, we only explicitly compare the LES to the particularly relevant, intriguing, and recent observations of Gargett and Savidge (2020). They report observations of the coastal ocean boundary layer in 31 m of water under a hurricane on the South Atlantic Bight. As in the simulation reported above, they observed the oceanic response to a hurricane that moved approximately northward and passed to the west of the observing tower over about a day. The maximum stress in their case is perhaps 50% weaker than in ours, but the temporal evolution is quite similar. The winds come from a fairly consistent direction as the storm approaches, they rotate rapidly and weaken as the eye passes, and then the winds stabilize their direction and intensify after the eye before weakening again.

Most interestingly, Gargett and Savidge (2020) also find coherent large rolls, which they attribute to Langmuir supercells that are strong as the storm approaches, wash away during

the eye passage, and then reemerge after the eye. The observed disappearance of the large rolls during the eye passage is qualitatively similar to the LES results above, although the observed forcing is dominated by waves whereas the LES forcing is dominated by winds, and their water column is essentially unstratified whereas ours is strongly stratified. A key conclusion of theirs, which our results seem to qualitatively endorse, is that steady-state nondimensional parameters may be insufficient to qualitatively or quantitatively characterize some features of OSBL turbulence under rapidly variable forcing. They also speculate that the disappearance of the large structures during the eye passage may reflect a sharp sensitivity to a ratio of two time scales: a time scale over which the large structures grow, and a time scale over which the mean flow or forcing evolves. This hypothesis is plausibly relevant in our LES as well, although the growth time scale of Ekman layer instabilities is thought to be much longer than Langmuir cells, and future work is necessary to test this hypothesis. We return to a discussion of the potential implications of missing surface waves in the LES below.

2) Kelvin–Helmholtz billows

The simulated large-scale structures just above the thermocline are also qualitatively similar to various oceanic observations of billows associated with shear instabilities in that they reveal temperature overturns wrapped by broken braids of strong vorticity that in some (rare) cases form cat's-eye patterns consistent with finite-amplitude Kelvin–Helmholtz billows in regions with a mean-profile $\mathrm{Ri}_g \approx 1/4$ (Seim and Gregg 1994; Chang et al. 2016). The crests and troughs of the simulated billows are oriented perpendicular to the mean shear vector at the depth of the thermocline, and their wavelength (about 125 m at the beginning of phase III) is consistent with the fastest growing linear KH instability on a canonical $\tanh(z/L)$ stratified shear layer with $L \approx 10$ m (Hazel 1972). However, the dominant-scale mode is also plausibly a result of merging or some other dynamical interaction and thereby associated with KH modes of a similar but different size [e.g., with half the wavelength and $L \approx 5$ m; see, e.g., Seim and Gregg (1994), Smyth and Moum (2000), and Smyth (2003)]. But, an exact match to theory is neither expected nor pursued since the observed mean shear and stratification are not exactly consistent with the canonical tanh profiles and the KH billows coexist with finite amplitude variance due to a range of other processes and scales (e.g., ambient turbulence lofted down from higher in the boundary layer; see Kaminski and Smyth 2019). Finally, it is worth reiterating that these billow-like structures are more the exception than the norm, although they are still directly responsible for ~10% of the covariances.

b. Missing processes

1) Surface gravity waves

Even though the SST cooling and rapid entrainment response to Hurricane Irene is qualitatively represented in the LES, one missing process that might significantly impact the OSBL turbulence described above is surface gravity waves. A future study with the Craik–Leibovich (CL) equations (e.g., McWilliams et al. 1997; Tejada-Martinez and Grosch 2007; Sullivan et al. 2012; Van Roekel et al. 2012; Large et al. 2019) might elucidate some effects of the time-dependent and misaligned waves and winds. Our omission of the wave effects captured by the CL equations might be cast as an assumption that the turbulent Langmuir number, i.e., $\mathrm{La}_t = \sqrt{u_*/u_s}$, where u_s is the surface Stokes velocity (Li et al. 2005), is sufficiently large. Although calculating the Stokes velocity for the wave field under Hurricane Irene is beyond the scope of this paper, La_t is likely within the range of 0.1–1 most of the time (e.g., as in the scenarios studied by Sullivan et al. 2012; Gargett and Savidge 2020), and thus CL effects are probably nonnegligible and likely dominant at some times. However, since the dominant waves (in the WaveWatch III simulation of Hurricane Irene; https://polar.ncep.noaa.gov/waves/hindcasts/prod-multi_1.php; Chawla et al. 2013) were often misaligned with the winds, which rotate rapidly, La_t itself may overestimate the CL effects (Van Roekel et al. 2012). In addition, there are other wave effects not captured by the CL equations that make it difficult to conjecture about the impact of waves in this scenario. For example, one issue is that the peak significant wave height is 8 m (in the WaveWatch III model) in 35 m of water, and the wave dynamics are in the intermediate regime (with peak wave periods ranging from about 14 to 7 s) where they are substantially modified by the shallow bottom. Further, wave-driven bottom boundary layer dynamics may also impact the evolution of the mean profiles (Grant and Madsen 1979, 1986) in ways not accounted for in either the LES reported here or an analogous simulation of the CL equations.

2) Pressure gradient forces and large-scale circulation

A second mechanism that may cause the OSBL turbulence to differ in the real ocean compared to the LES is the large-scale dynamics. In comparison to the surface waves, the effect of this process on the OSBL turbulence is more indirect, although probably more significant for the mean profile evolution and fluxes. In particular, pressure-gradient-driven flows arise due to the interactions of the wind-driven flow with the coastal boundary (e.g., Kundu et al. 1983; Glenn et al. 2016; Kelly 2019). As reported by Glenn et al. (2016), this process is likely responsible for both the observed stronger bottom velocity and weaker surface velocity relative to LES. In addition, the strong bottom flow activates the bottom boundary layer. Hence, mixing of the thermocline will occur both from below and above. Since the pressure gradient flows can induce a baroclinic response, they can both increase and decrease the vertical shear at the thermocline and could therefore reduce or increase mixing. Future work might evaluate the impact of the lateral pressure gradient forces on the OSBL turbulence in this scenario by imposing these forces, as simulated in the ocean model of Glenn et al. (2016), on the LES, and thereby build on the surface fluxes imposed in the control integration discussed here.

6. Conclusions

Hurricane Irene passed over the New Jersey Shelf on 28 August 2011. Ahead of the eye, wind-driven turbulent

mixing led to rapid cooling of the SST by over 4°C, which contributed to energy loss via air–sea heat flux from the hurricane to the ocean and the resulting rapid decay from category 3 to category 1 during 28 August (Glenn et al. 2016; Seroka et al. 2016). Here, we report a large-eddy simulation of the ocean turbulence at horizontal scales from 2 km to 1 m in a box of ocean just to the right of where the eye passed in the middle of the New Jersey shelf. The simulation was forced by our best estimates of the time-evolving air–sea heat and momentum fluxes during the storm and the analysis focuses on the period of time when the winds strengthen and then rapidly rotate as the storm approaches and passes; the poststorm period when the winds decay and the simulated surface boundary layer extends to the bottom is left for future work.

Despite the omission of surface gravity wave effects and large scale ocean circulation dynamics, the simulation captures the observed rapid ahead-of-eye cooling of SST and deepening of the surface mixed layer. The results show that the rapid ahead-of-eye cooling was due to two factors: 1) the shallow and sharp thermocline before the storm, which facilitates both a relatively rapid SST response for a given entrainment rate, as well as a relatively rapid entrainment rate for a given wind forcing, and 2) the magnitude of the wind stress, which supplies the energy for entrainment. However, the most striking feature of the simulation and the focus of the analysis is on ephemeral large coherent structures with aspect ratios ~10 that dominated the turbulent kinetic energy and buoyancy variance at various times and depths within the OSBL.

A descriptive analysis shows that the large-aspect-ratio structures have many similarities and some differences to the classic helical Ekman layer rolls in the top 5–10 m and Kelvin–Helmholtz billows just above the thermocline, both of which have been previously observed in the atmosphere and ocean and have a well-developed basis in linear instability theory. The simulated rolls have a peak characteristic speed of $\sim 10\,\mathrm{cm\,s^{-1}}$ and a wavelength of about 300 m just before the eye, only to be washed away by the rapid rotation of the wind as the eye passes. In addition, there is striking kilometer-scale spatial modulation of the KH billows in the thermocline, which are present to some degree at most times but have a growing dominant horizontal wavelength, are far from spatially ubiquitous, and have variable orientations and degrees of organization.

Analysis of the horizontal wavenumber spectra and cospectra allow us to separate and quantify the contribution of the large-scale structures to the turbulent kinetic energy and net vertical fluxes. We find that the large structures directly contribute more than half of the kinetic energy and buoyancy variance, ~10% of the total fluxes of momentum and buoyancy, and they may modify the turbulent Prandtl number by up to 50% (from say 1 to 1.5). Although these impacts on the mean profiles are substantial, the relatively small contribution of large scales to the total fluxes suggests that the large structures probably only modestly alter the mean profile evolution (by ~10%). Consistent with this suggestion, profiles of momentum flux, buoyancy flux, and the corresponding turbulent viscosity and diffusivity nearly collapse to time-independent profiles when appropriately nondimensionalized, despite the transient nature of the dynamics. Nevertheless, if the SST evolution in a similar model scenario is desired to within better than perhaps 0.5° (or about 10%), then the large-aspect-ratio structures are probably important to account for explicitly. The simulated large turbulent structures have some qualitative similarities to known linear instability models. Thus, these linear models may be a useful starting point for parameterization development, but future LES in other parts of parameter space are probably necessary to provide guidance and validation.

Finally, since this LES is an idealized process simulation, which omits potentially important surface gravity wave effects and larger-scale ocean circulation dynamics, caution should be exercised in extrapolating from these results to the real ocean. Although there are encouraging qualitative similarities between the LES and the observations of Gargett and Savidge (2020) of the coastal ocean response to a different hurricane, future simulations exploring the impacts of the missing processes in the LES as well as observational validation of the results presented here would be necessary to make robust conclusions about the dynamics of the large-aspect-ratio structures such as those simulated here under a hurricane. As mentioned above, such future efforts may be warranted if models of the SST evolution under a hurricane are desired to within 10% accuracy.

Acknowledgments. This material is based upon work supported by the National Center for Atmospheric Research, which is a major facility sponsored by the National Science Foundation (NSF) under Cooperative Agreement 1852977. Computing and data storage resources, including the Cheyenne supercomputer (doi:10.5065/D6RX99HX), were provided by the Computational and Information Systems Laboratory at NCAR. CEW acknowledges support from Rutgers University through the School of Environmental and Biological Sciences Excellence Fellowship and the Teledyne Webb Research Graduate Fellowship. CEW also appreciates the guidance and patience of his advisor Scott Glenn as well as the insights of Bill Large, Bob Chant, Melissa Moulton, Jenessa Duncombe, and Sonya Legg into the dynamics of the system. DBW acknowledges support from the NSF, via OPP-1501993 and OCE-1658541, NOAA, via NA18OAR4310408, and NASA, via 80NSSC19K1116.

Data availability statement. All data used in this paper are publicly available in a cited reference or in Watkins and Whitt (2020); https://doi.org/10.6084/m9.figshare.12486056.v5.

REFERENCES

Anderson, P. S., 2009: Measurement of Prandtl number as a function of Richardson number avoiding self-correlation. *Bound.-Layer Meteor.*, **131**, 345–362, https://doi.org/10.1007/s10546-009-9376-4.

Anis, A., and J. Moum, 1995: Surface wave–turbulence interactions. scaling ε (z) near the sea surface. *J. Phys. Oceanogr.*, **25**, 2025–2045, https://doi.org/10.1175/1520-0485(1995)025<2025:SWISNT>2.0.CO;2.

Asai, T. and I. Nakasuji, 1973: On the stability of Ekman boundary layer flow with thermally unstable stratification. *J. Meteor.*

Soc. Japan, **51**, 29–42, https://doi.org/10.2151/jmsj1965.51.1_29.

Brown, R. A., 1972: On the inflection point instability of a stratified Ekman boundary layer. *J. Atmos. Sci.*, **29**, 850–859, https://doi.org/10.1175/1520-0469(1972)029<0850:OTIPIO>2.0.CO;2.

Businger, J. A., J. C. Wyngaard, Y. Izumi, and E. F. Bradley, 1971: Flux-profile relationships in the atmospheric surface layer. *J. Atmos. Sci.*, **28**, 181–189, https://doi.org/10.1175/1520-0469(1971)028<0181:FPRITA>2.0.CO;2.

Callies, J., and R. Ferrari, 2018: Baroclinic instability in the presence of convection. *J. Phys. Oceanogr.*, **48**, 45–60, https://doi.org/10.1175/JPO-D-17-0028.1.

Chang, M.-H., S.-Y. Jheng, and R.-C. Lien, 2016: Trains of large Kelvin-Helmholtz billows observed in the Kuroshio above a seamount. *Geophys. Res. Lett.*, **43**, 8654–8661, https://doi.org/10.1002/2016GL069462.

Chawla, A., D. M. Spindler, and H. L. Tolman, 2013: Validation of a thirty year wave hindcast using the Climate Forecast System Reanalysis winds. *Ocean Modell.*, **70**, 189–206, https://doi.org/10.1016/j.ocemod.2012.07.005.

Czeschel, L., and C. Eden, 2019: Internal wave radiation through surface mixed layer turbulence. *J. Phys. Oceanogr.*, **49**, 1827–1844, https://doi.org/10.1175/JPO-D-18-0214.1.

D'Asaro, E. A., and Coauthors, 2018: Ocean convergence and the dispersion of flotsam. *Proc. Natl. Acad. Sci. USA*, **115**, 1162–1167, https://doi.org/10.1073/pnas.1718453115.

Deusebio, E., G. Brethouwer, P. Schlatter, and E. Lindborg, 2014: A numerical study of the unstratified and stratified Ekman layer. *J. Fluid Mech.*, **755**, 672–704, https://doi.org/10.1017/jfm.2014.318.

Duncombe, J. R., 2017: Linear theory of roll instabilities in the ocean surface layer. M.S. thesis, Dept. of Ocean, Earth, and Atmospheric Sciences, Oregon State University, 76 pp.

Ekman, V. W., 1905: On the influence of the earth's rotation on ocean currents. *Ark. Mat. Astr. Fys.*, **2**, 1–52.

Elachi, C., and J. R. Apel, 1976: Internal wave observations made with an airborne synthetic aperture imaging radar. *Geophys. Res. Lett.*, **3**, 647–650, https://doi.org/10.1029/GL003i011p00647.

Etling, D., and R. Brown, 1993: Roll vortices in the planetary boundary layer: A review. *Bound.-Layer Meteor.*, **65**, 215–248, https://doi.org/10.1007/BF00705527.

Fairall, C. W., E. F. Bradley, J. Hare, A. A. Grachev, and J. B. Edson, 2003: Bulk parameterization of air–sea fluxes: Updates and verification for the COARE algorithm. *J. Climate*, **16**, 571–591, https://doi.org/10.1175/1520-0442(2003)016<0571:BPOASF>2.0.CO;2.

Fang, J., and F. Porté-Agel, 2015: Large-eddy simulation of very-large-scale motions in the neutrally stratified atmospheric boundary layer. *Bound.-Layer Meteor.*, **155**, 397–416, https://doi.org/10.1007/s10546-015-0006-z.

Gargett, A. E., J. Wells, A. Tejada-Martinez, and C. Grosch, 2004: Langmuir supercells: A mechanism for sediment resuspension and transport in shallow seas. *Science*, **306**, 1925–1928, https://doi.org/10.1126/science.1100849.

——, and D. K. Savidge, 2020: Winds, waves, and turbulence on a shallow continental shelf during passage of a tropical storm. *J. Phys. Oceanogr.*, **50**, 1341–1364, https://doi.org/10.1175/JPO-D-20-0024.1.

Glenn, S., and Coauthors, 2016: Stratified coastal ocean interactions with tropical cyclones. *Nat. Commun.*, **7**, 10887, https://doi.org/10.1038/ncomms10887.

Grant, W. D., and O. S. Madsen, 1979: Combined wave and current interaction with a rough bottom. *J. Geophys. Res.*, **84**, 1797–1808, https://doi.org/10.1029/JC084iC04p01797.

——, and ——, 1986: The continental-shelf bottom boundary layer. *Annu. Rev. Fluid Mech.*, **18**, 265–305, https://doi.org/10.1146/annurev.fl.18.010186.001405.

Hamlington, P. E., L. P. VanRoekel, B. Fox-Kemper, K. Julien, and G. Chini, 2014: Langmuir–submesoscale interactions: Descriptive analysis of multiscale frontal spindown simulations. *J. Phys. Oceanogr.*, **44**, 2249–2272, https://doi.org/10.1175/JPO-D-13-0139.1.

Hazel, P., 1972: Numerical studies of the stability of inviscid stratified shear flows. *J. Fluid Mech.*, **51**, 39–61, https://doi.org/10.1017/S0022112072001065.

Holt, S. E., J. R. Koseff, and J. H. Ferziger, 1992: A numerical study of the evolution and structure of homogeneous stably stratified sheared turbulence. *J. Fluid Mech.*, **237**, 499–539, https://doi.org/10.1017/S0022112092003513.

Howard, L. N., 1961: Note on a paper of John W. Miles. *J. Fluid Mech.*, **10**, 509–512, https://doi.org/10.1017/S0022112061000317.

Hutchins, N., K. Chauhan, I. Marusic, J. Monty, and J. Klewicki, 2012: Towards reconciling the large-scale structure of turbulent boundary layers in the atmosphere and laboratory. *Bound.-Layer Meteor.*, **145**, 273–306, https://doi.org/10.1007/s10546-012-9735-4.

Kaltenbach, H.-J., T. Gerz, and U. Schumann, 1994: Large-eddy simulation of homogeneous turbulence and diffusion in stably stratified shear flow. *J. Fluid Mech.*, **280**, 1–40, https://doi.org/10.1017/S0022112094002831.

Kaminski, A., and W. Smyth, 2019: Stratified shear instability in a field of pre-existing turbulence. *J. Fluid Mech.*, **862**, 639–658, https://doi.org/10.1017/jfm.2018.973.

Kaylor, R., and A. J. Faller, 1972: Instability of the stratified Ekman boundary layer and the generation of internal waves. *J. Atmos. Sci.*, **29**, 497–509, https://doi.org/10.1175/1520-0469(1972)029<0497:IOTSEB>2.0.CO;2.

Kelly, S. M., 2019: Coastally generated near-inertial waves. *J. Phys. Oceanogr.*, **49**, 2979–2995, https://doi.org/10.1175/JPO-D-18-0148.1.

Khanna, S., and J. G. Brasseur, 1998: Three-dimensional buoyancy- and shear-induced local structure of the atmospheric boundary layer. *J. Atmos. Sci.*, **55**, 710–743, https://doi.org/10.1175/1520-0469(1998)055<0710:TDBASI>2.0.CO;2.

Kukulka, T., A. J. Plueddemann, J. H. Trowbridge, and P. P. Sullivan, 2009: Significance of Langmuir circulation in upper ocean mixing: Comparison of observations and simulations. *Geophys. Res. Lett.*, **36**, L10603, https://doi.org/10.1029/2009GL037620.

Kundu, P. K., S.-Y. Chao, and J. P. McCreary, 1983: Transient coastal currents and inertio-gravity waves. *Deep-Sea Res.*, **30A**, 1059–1082, https://doi.org/10.1016/0198-0149(83)90061-4.

Langmuir, I., 1938: Surface motion of water induced by wind. *Science*, **87**, 119–123, https://doi.org/10.1126/science.87.2250.119.

Large, W. G., J. C. McWilliams, and S. C. Doney, 1994: Oceanic vertical mixing: A review and a model with a nonlocal boundary layer parameterization. *Rev. Geophys.*, **32**, 363–403, https://doi.org/10.1029/94RG01872.

——, E. G. Patton, and P. P. Sullivan, 2019: Nonlocal transport and implied viscosity and diffusivity throughout the boundary layer in LES of the Southern Ocean with surface waves. *J. Phys. Oceanogr.*, **49**, 2631–2652, https://doi.org/10.1175/JPO-D-18-0202.1.

Leibovich, S., 1983: The form and dynamics of Langmuir circulations. *Annu. Rev. Fluid Mech.*, **15**, 391–427, https://doi.org/10.1146/annurev.fl.15.010183.002135.

Lemone, M. A., 1973: The structure and dynamics of horizontal roll vortices in the planetary boundary layer. *J. Atmos. Sci.*, **30**, 1077–1091, https://doi.org/10.1175/1520-0469(1973)030<1077:TSADOH>2.0.CO;2.

——, 1976: Modulation of turbulence energy by longitudinal rolls in an unstable planetary boundary layer. *J. Atmos. Sci.*, **33**, 1308–1320, https://doi.org/10.1175/1520-0469(1976)033<1308:MOTEBL>2.0.CO;2.

Li, M., C. Garrett, and E. Skyllingstad, 2005: A regime diagram for classifying turbulent large eddies in the upper ocean. *Deep-Sea Res. I*, **52**, 259–278, https://doi.org/10.1016/j.dsr.2004.09.004.

Lombardo, C., and M. Gregg, 1989: Similarity scaling of viscous and thermal dissipation in a convecting surface boundary layer. *J. Geophys. Res.*, **94**, 6273–6284, https://doi.org/10.1029/JC094iC05p06273.

Marmorino, G., and W. Chen, 2019: Use of WorldView-2 along-track stereo imagery to probe a Baltic Sea algal spiral. *Remote Sens.*, **11**, 865, https://doi.org/10.3390/rs11070865.

——, G. Smith, and G. Lindemann, 2005: Infrared imagery of large-aspect-ratio Langmuir circulation. *Cont. Shelf Res.*, **25** (1), 1–6, https://doi.org/10.1016/j.csr.2004.08.002.

Marusic, I., B. J. McKeon, P. A. Monkewitz, H. M. Nagib, A. J. Smits, and K. R. Sreenivasan, 2010: Wall-bounded turbulent flows at high Reynolds numbers: Recent advances and key issues. *Phys. Fluids*, **22**, 065103, https://doi.org/10.1063/1.3453711.

McWilliams, J. C., P. P. Sullivan, and C.-H. Moeng, 1997: Langmuir turbulence in the ocean. *J. Fluid Mech.*, **334**, 1–30, https://doi.org/10.1017/S0022112096004375.

Merckelbach, L., A. Berger, G. Krahmann, M. Dengler, and J. R. Carpenter, 2019: A dynamic flight model for slocum gliders and implications for turbulence microstructure measurements. *J. Atmos. Oceanic Technol.*, **36**, 281–296, https://doi.org/10.1175/JTECH-D-18-0168.1.

Miles, J. W., 1961: On the stability of heterogeneous shear flows. *J. Fluid Mech.*, **10**, 496–508, https://doi.org/10.1017/S0022112061000305.

Moeng, C.-H., and P. P. Sullivan, 1994: A comparison of shear-and buoyancy-driven planetary boundary layer flows. *J. Atmos. Sci.*, **51**, 999–1022, https://doi.org/10.1175/1520-0469(1994)051<0999:ACOSAB>2.0.CO;2.

Monin, A. S., and A. M. Obukhov, 1954: Basic laws of turbulent mixing in the surface layer of the atmosphere. *Tr. Geofiz. Inst., Akad. Nauk SSSR*, **24**, 163–187.

Munk, W., L. Armi, K. Fischer, and F. Zachariasen, 2000: Spirals on the sea. *Proc. Roy. Soc. London*, **456A**, 1217–1280, https://doi.org/10.1098/rspa.2000.0560.

Osborn, T., 1980: Estimates of the local rate of vertical diffusion from dissipation measurements. *J. Phys. Oceanogr.*, **10**, 83–89, https://doi.org/10.1175/1520-0485(1980)010<0083:EOTLRO>2.0.CO;2.

Paulson, C. A., and J. J. Simpson, 1977: Irradiance measurements in the upper ocean. *J. Phys. Oceanogr.*, **7**, 952–956, https://doi.org/10.1175/1520-0485(1977)007<0952:IMITUO>2.0.CO;2.

Pollard, R. T., and R. C. Millard, 1970: Comparison between observed and simulated wind-generated inertial oscillations. *Deep-Sea Res. Oceanogr. Abstr.*, **17**, 813–821, https://doi.org/10.1016/0011-7471(70)90043-4.

——, P. B. Rhines, and R. Thompson, 1972: The deepening of the wind-mixed layer. *Geophys. Fluid Dyn.*, **4**, 381–404, https://doi.org/10.1080/03091927208236105.

Polton, J. A., J. A. Smith, J. A. MacKinnon, and A. E. Tejada-Martínez, 2008: Rapid generation of high-frequency internal waves beneath a wind and wave forced oceanic surface mixed layer. *Geophys. Res. Lett.*, **35**, L13602, https://doi.org/10.1029/2008GL033856.

Rohr, J., E. Itsweire, K. Helland, and C. Van Atta, 1988: Growth and decay of turbulence in a stably stratified shear flow. *J. Fluid Mech.*, **195**, 77–111, https://doi.org/10.1017/S0022112088002332.

Savelyev, I., and Coauthors, 2018a: Aerial observations of symmetric instability at the north wall of the Gulf Stream. *Geophys. Res. Lett.*, **45**, 236–244, https://doi.org/10.1002/2017GL075735.

——, and Coauthors, 2018b: Airborne remote sensing of the upper ocean turbulence during CASPER-East. *Remote Sens.*, **10**, 1224, https://doi.org/10.3390/rs10081224.

Seim, H. E., and M. C. Gregg, 1994: Detailed observations of a naturally occurring shear instability. *J. Geophys. Res.*, **99**, 10 049–10 073, https://doi.org/10.1029/94JC00168.

Seroka, G., T. Miles, Y. Xu, J. Kohut, O. Schofield, and S. Glenn, 2016: Hurricane Irene sensitivity to stratified coastal ocean cooling. *Mon. Wea. Rev.*, **144**, 3507–3530, https://doi.org/10.1175/MWR-D-15-0452.1.

Shaun-Johnston, T. M., and D. L. Rudnick, 2009: Observations of the transition layer. *J. Phys. Oceanogr.*, **39**, 780–797, https://doi.org/10.1175/2008JPO3824.1.

Skyllingstad, E. D., and R. Samelson, 2012: Baroclinic frontal instabilities and turbulent mixing in the surface boundary layer. Part I: Unforced simulations. *J. Phys. Oceanogr.*, **42**, 1701–1716, https://doi.org/10.1175/JPO-D-10-05016.1.

——, J. Duncombe, and R. M. Samelson, 2017: Baroclinic frontal instabilities and turbulent mixing in the surface boundary layer. Part II: Forced simulations. *J. Phys. Oceanogr.*, **47**, 2429–2454, https://doi.org/10.1175/JPO-D-16-0179.1.

Smith, J. A., 1992: Observed growth of Langmuir circulation. *J. Geophys. Res.*, **97**, 5651–5664, https://doi.org/10.1029/91JC03118.

Smith, K. M., P. E. Hamlington, and B. Fox-Kemper, 2016: Effects of submesoscale turbulence on ocean tracers. *J. Geophys. Res.*, **121**, 908–933, https://doi.org/10.1002/2015JC011089.

Smits, A. J., B. J. McKeon, and I. Marusic, 2011: High-Reynolds number wall turbulence. *Annu. Rev. Fluid Mech.*, **43**, 353–375, https://doi.org/10.1146/annurev-fluid-122109-160753.

Smyth, W., J. Nash, and J. Moum, 2019: Self-organized criticality in geophysical turbulence. *Sci. Rep.*, **9**, 3747, https://doi.org/10.1038/s41598-019-39869-w.

Smyth, W. D., 2003: Secondary Kelvin–Helmholtz instability in weakly stratified shear flow. *J. Fluid Mech.*, **497**, 67–98, https://doi.org/10.1017/S0022112003006591.

——, and J. N. Moum, 2000: Length scales of turbulence in stably stratified mixing layers. *Phys. Fluids*, **12**, 1327–1342, https://doi.org/10.1063/1.870385.

Sous, D., J. Sommeria, and D. Boyer, 2013: Friction law and turbulent properties in a laboratory Ekman boundary layer. *Phys. Fluids*, **25**, 046602, https://doi.org/10.1063/1.4802045.

Stevenson, J. W., and P. P. Niiler, 1983: Upper ocean heat budget during the Hawaii-to-Tahiti shuttle experiment. *J. Phys. Oceanogr.*, **13**, 1894–1907, https://doi.org/10.1175/1520-0485(1983)013<1894:UOHBDT>2.0.CO;2.

Sullivan, P. P., and J. C. McWilliams, 2018: Frontogenesis and frontal arrest of a dense filament in the oceanic surface boundary layer. *J. Fluid Mech.*, **837**, 341–380, https://doi.org/10.1017/jfm.2017.833.

——, and ——, 2019: Langmuir turbulence and filament frontogenesis in the oceanic surface boundary layer. *J. Fluid Mech.*, **879**, 512–553, https://doi.org/10.1017/jfm.2019.655.

——, L. Romero, J. C. McWilliams, and W. K. Melville, 2012: Transient evolution of Langmuir turbulence in ocean boundary layers driven by hurricane winds and waves. *J. Phys. Oceanogr.*, **42**, 1959–1980, https://doi.org/10.1175/JPO-D-12-025.1.

Sundermeyer, M. A., E. Skyllingstad, J. R. Ledwell, B. Concannon, E. A. Terray, D. Birch, S. D. Pierce, and B. Cervantes, 2014: Observations and numerical simulations of large-eddy circulation in the ocean surface mixed layer. *Geophys. Res. Lett.*, **41**, 7584–7590, https://doi.org/10.1002/2014GL061637.

Tatro, P. R., and E. Mollo-Christensen, 1967: Experiments on Ekman layer instability. *J. Fluid Mech.*, **28**, 531–543, https://doi.org/10.1017/S0022112067002289.

Taylor, J. R., 2016: Turbulent mixing, restratification, and phytoplankton growth at a submesoscale eddy. *Geophys. Res. Lett.*, **43**, 5784–5792, https://doi.org/10.1002/2016GL069106.

——, 2008: Numerical simulations of the stratified oceanic bottom boundary layer. Ph.D. dissertation, University of California, San Diego, 230 pp.

Tejada-Martinez, A., and C. Grosch, 2007: Langmuir turbulence in shallow water. Part II. Large-eddy simulation. *J. Fluid Mech.*, **576**, 63–108, https://doi.org/10.1017/S0022112006004587.

Thorpe, S., 2002: The axial coherence of Kelvin–Helmholtz billows. *Quart. J. Roy. Meteor. Soc.*, **128**, 1529–1542, https://doi.org/10.1002/qj.200212858307.

——, 2004: Langmuir circulation. *Annu. Rev. Fluid Mech.*, **36**, 55–79, https://doi.org/10.1146/annurev.fluid.36.052203.071431.

——, and Z. Liu, 2009: Marginal instability? *J. Phys. Oceanogr.*, **39**, 2373–2381, https://doi.org/10.1175/2009JPO4153.1.

Turner, J. S., 1979: *Buoyancy Effects in Fluids*. Cambridge University Press, 368 pp.

Van Roekel, L., B. Fox-Kemper, P. Sullivan, P. Hamlington, and S. Haney, 2012: The form and orientation of Langmuir cells for misaligned winds and waves. *J. Geophys. Res.*, **117**, C05001, https://doi.org/10.1029/2011JC007516.

Venayagamoorthy, S. K., and J. R. Koseff, 2016: On the flux Richardson number in stably stratified turbulence. *J. Fluid Mech.*, **798**, R1, https://doi.org/10.1017/jfm.2016.340.

Watkins, C., and D. Whitt, 2020: Data for large-aspect-ratio structures in simulated ocean surface boundary layer turbulence under a hurricane. Figshare, accessed 16 June 2020, https://doi.org/10.6084/m9.figshare.12486056.v5.

Whitt, D. B., and J. R. Taylor, 2017: Energetic submesoscales maintain strong mixed layer stratification during an autumn storm. *J. Phys. Oceanogr.*, **47**, 2419–2427, https://doi.org/10.1175/JPO-D-17-0130.1.

——, M. Lévy, and J. R. Taylor, 2019: Submesoscales enhance storm-driven vertical mixing of nutrients: Insights from a biogeochemical large eddy simulation. *J. Geophys. Res. Oceans*, **124**, 8140–8165, https://doi.org/10.1029/2019JC015370.

Wijesekera, H. W., and T. M. Dillon, 1991: Internal waves and mixing in the upper equatorial Pacific Ocean. *J. Geophys. Res.*, **96**, 7115–7125, https://doi.org/10.1029/90JC02727.

Young, G. S., D. A. Kristovich, M. R. Hjelmfelt, and R. C. Foster, 2002: Rolls, streets, waves, and more: A review of quasi-two-dimensional structures in the atmospheric boundary layer. *Bull. Amer. Meteor. Soc.*, **83**, 997–1002, https://doi.org/10.1175/1520-0477(2002)083<0997:RSWAMA>2.3.CO;2.